Check for updates

Permafrost and Periglacial Processes

WILEY

RESEARCH ARTICLE

Permafrost Thaw Drives Iron and Organic Carbon Release Into Soil Pore Water During Palsa to Degraded Palsa Transition

Eléonore du Bois d'Aische[1,2] | François Jonard[1,2] | Catherine Hirst[1,3] | Maëlle Villani[1] | Maxime Thomas[1] | Reiner Giesler[4] | Carl-Magnus Mörth[5] | Erik Lundin[6] | Kristof Van Oost[1] | Veerle Vanacker[1,7] | Sébastien Lambot[1] | Sophie Opfergelt[1]

[1]Earth and Life Institute, Université Catholique de Louvain, Louvain-la-Neuve, Belgium | [2]Earth Observation and Ecosystem Modelling Laboratory, SPHERES Research Unit, Université de Liège, Liège, Belgium | [3]Department of Earth Sciences, Durham University, Durham, UK | [4]Climate Impacts Research Centre, Department of Ecology and Environmental Science, Umeå University, Umeå, Sweden | [5]Department of Geological Sciences, Stockholm University, Stockholm, Sweden | [6]Abisko Scientific Research Station, Swedish Polar Research Secretariat, Abisko, Sweden | [7]Soil Geography and Landscape Group, Wageningen University, Wageningen, The Netherlands

Correspondence: Eléonore du Bois d'Aische (eleonore.dubois@uclouvain.be)

Received: 19 December 2024 | **Revised:** 13 October 2025 | **Accepted:** 6 November 2025

Funding: This work was supported by European Research Council (714617), Fédération Wallonie-Bruxelles (21/26-119), and Fonds De La Recherche Scientifique - FNRS (FC54613, FC69480, FC49507).

Keywords: iron | organic carbon | permafrost | soil water content

ABSTRACT

Permafrost degradation, driven by rising temperatures in high-latitude regions, destabilizes previously sequestered soil organic carbon (OC), increasing greenhouse gas emissions and amplifying global warming. In these ecosystems, interactions with mineral surfaces and metal oxides, particularly iron (Fe), stabilize up to 80% of soil OC. This study investigates the mechanisms of Fe solubilization and OC release across a permafrost thaw gradient in Stordalen, Abisko, Sweden, including palsa, intermediate, and highly degraded permafrost stages. By integrating geophysical measurements—including relative elevation, thaw depth, soil water content, and soil temperature with redox potential and soil pore water chemistry, we identify the environmental conditions driving iron and organic carbon release into soil pore waters with permafrost degradation. Our results show that combining relative elevation, thaw depth, soil water content, soil pore water pH, and soil pore water conductivity with shifts in vegetation species enables very-high-resolution detection of permafrost degradation at submeter scales, distinguishing intact from degraded permafrost soils. We show that small-scale changes in thaw depth and water content alter soil pH and redox conditions, driving the release of Fe and dissolved organic carbon (DOC) and promoting the formation of Fe-DOC complexes in soil pore water. The amount of exported Fe-DOC complexes from thawed soils varies with the stage of permafrost degradation, and the fate of Fe-DOC complexes is likely to evolve along the soil–stream continuum. This study highlights how environmental conditions upon thaw control the type of Fe-DOC association in soil pore waters, a parameter to consider when quantifying what DOC is available for microbial and photo-degradation in aquatic systems which are significant sources of greenhouse gas emissions across Arctic landscapes.

© 2025 John Wiley & Sons Ltd.

1 | Introduction

Permafrost in high latitude regions constitutes a substantial reservoir of organic carbon on Earth, storing 1460–1600 Pg [1, 2]. The soil carbon from the top 3 m of permafrost soils accounts for 50% of the total stock of carbon [3]. This reservoir is increasingly recognized as a critical component of the global carbon cycle and is prone to change in the context of contemporary global warming with a projected loss of permafrost volume of more than 50% by 2100 if global temperatures rise by 1.5°C–2.0°C [4]. As global air temperatures rise, permafrost degradation accelerates, releasing previously sequestered carbon in the form of greenhouse gases, particularly carbon dioxide and methane. This process initiates a positive feedback loop, exacerbating the increase in air temperature and thus accelerating permafrost thaw [4]. The Intergovernmental Panel on Climate Change report (2022) highlights that thawing permafrost significantly contributes to global greenhouse gas emissions, underscoring the critical role of permafrost carbon feedback in driving rising atmospheric CO_2 levels. The implications further extend beyond greenhouse gas emissions, encompassing alterations in Arctic ecosystems and landscapes.

Arctic peatlands, characterized by the accumulation of partially decayed organic matter in waterlogged conditions, represent an integral component of the Arctic landscape, playing a crucial role in regional carbon dynamics and ecosystem functioning. These peatlands are widespread across the Arctic region, encompassing vast areas in northern latitudes [5–7]. The cold, waterlogged conditions prevalent in the Arctic limit the decomposition of organic matter, fostering the accumulation of peat over time. This peatland carbon stock is increasingly susceptible to climate change–induced warming, potentially leading to permafrost thaw and subsequent carbon release [8–11]. Palsa mires, a distinctive type of frozen peatland, emerge from frost heaving and thermokarst processes [12–14]. Frost heaving contributes to the formation of elevated peat plateaus known as palsas, while thermokarst exacerbates ground subsidence in the surrounding areas, creating depressions when the underlying permafrost thaws. These degraded palsas or collapsed palsas are also referred to as fen [15–18]. This difference in elevation between palsa and degraded palsa influences surface hydrology and creates distinct submeter scale environments with contrasting moisture and nutrient characteristics that, in turn, support contrasting vegetation types [19–21]. The palsa mire comprises ombrotrophic elevated hummocks with a shallow active layer mainly dominated by lichens, rhizomatic plants such as *Rubus chamaemorus*, and small shrubs. In contrast, the minerotrophic depressions are dominated by sedges such as *Eriophorum vaginatum*, and mosses such as *Sphagnum* sp. [16, 19, 22–27]. The distinctive vegetation types result in topography-controlled landcover distributions [28, 29]. Due to the slow adaptation of vegetation species to environmental changes, such as those caused by hydrological shifts or permafrost thaw [30, 31], using only vegetation type as an indicator of active layer depth may lead to underestimation of the stage of permafrost degradation at the landscape scale. Although vegetation distribution may reflect different stages of permafrost degradation, it fails to detect stages of palsa degradation, where a deepening active layer occurs without visible changes in the vegetation community. This is because vegetation lags in responding to changes in habitat conditions, such as soil depth and water content, creating a temporal window where vegetation adapted to earlier degradation stages persists despite ongoing permafrost thaw.

The stages of permafrost degradation are characterized by distinct hydrological regimes. Palsa soils contain relatively low soil pore water content when unfrozen during summer months, while degraded palsa soils and sediments are water-saturated [15]. The variation in soil water content (SWC) influences the availability of electron acceptors and donors, consequently shaping the redox state of the soil and affecting pH levels [32]. Higher SWC often corresponds to reduced redox potential (Eh), fostering anaerobic conditions, while lower SWC promotes oxidized conditions [8, 33, 34]. Moreover, in peatland environments, which are acidic with pH values typically ranging from 3 to 5, this acidity results from the accumulation of organic acids produced during the decomposition of plant material under low mineralization rates [35–37], resulting from anaerobic conditions fostered by high SWC. Conversely, when water content decreases (e.g., due to drainage), the peat can become more aerobic, potentially increasing pH levels as organic acids are mineralized. However, in the context of Arctic peatlands, higher SWC tends to elevate pH through enhanced ion mobility and leaching of cations, while decreased SWC is associated with more acidic conditions [33, 38]. Following changes in SWC, pH, and redox potential is crucial for understanding the geochemical dynamics of these Arctic peatland soils. These factors have significant implications for the dynamics of soil organic carbon (SOC), and the release of more mobile organic molecules as dissolved organic carbon (DOC), a carbon pool more readily available for microorganisms [39, 40].

A portion of permafrost SOC is associated with iron (Fe) bearing minerals [41–43]. Those associations result from complexation, sorption, and aggregation of SOC and Fe, all of which contribute to preserving SOC from decomposition [44–49]. The stability of the organo-mineral interactions involving iron-bearing minerals is critically dependent on the physicochemical conditions, particularly pH and redox potential, and is strongly influenced by the nature of the iron minerals involved [34, 41, 50, 51]. Poorly crystalline iron oxides such as ferrihydrite play a dominant role in SOC stabilization compared with crystalline iron oxides, such as goethite and hematite [52–54]. Ferrihydrite is more reactive due to its large specific surface area and numerous reactive sites, allowing it to adsorb and coprecipitate more SOC relative to crystalline iron oxides [46, 47, 55–57]. However, ferrihydrite is highly sensitive to reducing conditions, where ferric iron (Fe^{3+}) is reduced to ferrous iron (Fe^{2+}). This reduction can destabilize the mineral structure and release the associated OC into the soil solution, particularly in waterlogged or anaerobic environments [54, 58]. In contrast, crystalline iron oxides are more resistant to redox fluctuations, providing a more stable environment for OC retention. In addition, acidic soil conditions enhance the solubility of iron, promoting the formation of poorly crystalline minerals like ferrihydrite, which in turn increases the capacity for SOC stabilization [58]. In acidic DOC-rich soil solutions, Fe forms Fe-DOC complexes or ferrihydrite-DOC coprecipitates [59–61] and the amount and composition of DOC bound to Fe may mediate DOC fate in aquatic bodies [59, 62, 63]. This motivates the need to constrain how changes in soil pH–Eh upon permafrost thaw modulate the release of Fe and DOC from soils into soil pore waters.

10991530, 0, Downloaded from https://onlinelibrary.wiley.com/doi/10.1002/ppp.70018 by Université De Liège, Wiley Online Library on [27/11/2025]. See the Terms and Conditions (https://onlinelibrary.wiley.com/terms-and-conditions) on Wiley Online Library for rules of use; OA articles are governed by the applicable Creative Commons License

Peatland soils from palsa mires facing permafrost thaw represent a natural laboratory with contrasting permafrost conditions (e.g., thaw depth and elevation) and hydrological conditions (soil moisture) to investigate the influence of the associated changing geochemical conditions (pH–Eh) on the Fe and DOC release. Our hypotheses are that (a) the combination of thaw depth, elevation, SWC (geophysical parameters) and soil pore water chemistry (geochemical parameters) allows a submeter scale identification of the state of the underlying permafrost within a thawing sequence, and (b) permafrost degradation drives iron and organic carbon release from soil to soil pore waters and the binding between iron and organic carbon in soil pore water. To test our hypotheses, we studied a permafrost thawing gradient in Stordalen mire, an Arctic peatland in Northern Sweden. The thawing gradient enables a space-for-time approach: We sampled the two end members of the permafrost degradation process, that is, a palsa with a shallow permafrost table and a degraded palsa comprising degraded permafrost, as well as an intermediate stage. We assess the evolution of Fe and DOC release in soil pore water along that gradient.

2 | Materials and Methods

2.1 | Study Site

Stordalen Mire is a frozen peatland located 200 km north of the Arctic Circle (68°21′ N, 18°49′ E; Figure 1a,b). It is underlain by a granitic bedrock covered by a lacustrine deposit composed mainly of silt of glacial origins [64]. The formation of peat in Stordalen Mire started more than 5000 years ago, and the peat layer had a mean thickness of 0.5 m in 2009 [64, 65]. Encompassing an area of 25 ha, Stordalen Mire displays a sub-Arctic tundra environment characterized by discontinuous permafrost [64, 66]. The discontinuous distribution of permafrost gives rise to small-scale variation in surface topography, characterized by elevation differences of less than 2 m over short meter-scale distances typical of a palsa mire. The climate data sourced from the Abisko Scientific Research Station indicate a positive mean air temperature of 0.06°C in 2006 and reveal a 2.5 °C rise in mean annual air temperature between 1913 and 2006 [67]. This temperature increase has resulted in deeper summer thaw depth and the disappearance of permafrost in specific areas of

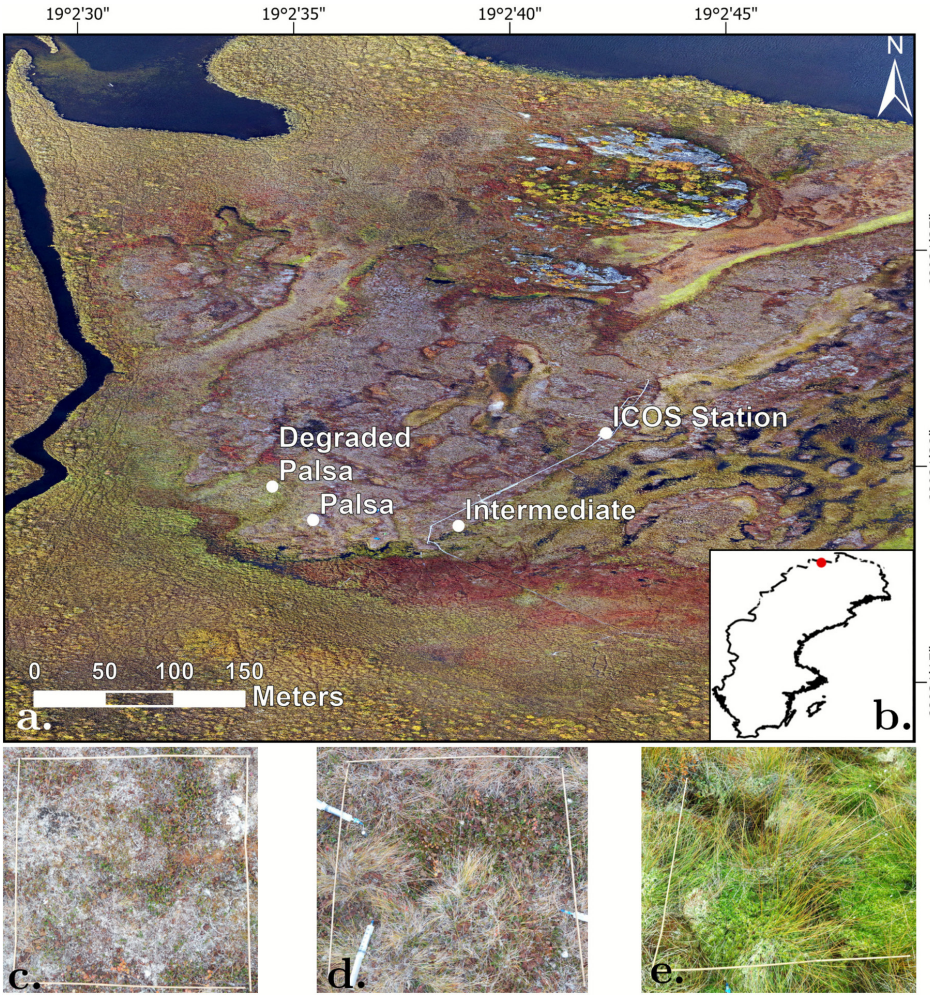

FIGURE 1 | Orthomosaic of Stordalen Mire (WGS 1984) (a) and its location in Sweden (red point; b). The map illustrates the localization of the three sampling sites (palsa (c), intermediate (d), and degraded palsa (e)). More specifically, (c), (d), and (e), illustrate the vegetation community of each specific sampling site within the square of 1 × 1 m. [Colour figure can be viewed at wileyonlinelibrary.com]

10991530, 0, Downloaded from https://onlinelibrary.wiley.com/doi/10.1002/ppp.70018 by Université De Liège, Wiley Online Library on [27/11/2025]. See the Terms and Conditions (https://onlinelibrary.wiley.com/terms-and-conditions) on Wiley Online Library for rules of use; OA articles are governed by the applicable Creative Commons License

Stordalen [68]. We investigate the two end-members of the palsa mire (palsa and degraded palsa) as well as an intermediate stage of the permafrost degradation process during the late shoulder season. These three sampling sites will be respectively referred to as palsa, intermediate, and degraded palsa. The locations of the two end-members, that is, palsa and degraded palsa, were chosen based on their distinct vegetation communities, constituting, with thaw depth, the selection criteria for these two sites [16, 19, 27]. The palsa site corresponds to lichen hummock types, primarily consisting of lichens and *Betula nana* (Figure 1c) whereas the degraded palsa features vegetation characteristic of tall graminoids, with species like *Eriophorum vaginatum*, *Epilobium angustifolium*, and *Sphagnum* mosses prevalent (Figure 1e). The intermediate stage is characterized by the presence of permafrost, but with a deeper thaw depth than at the palsa. At this site, the vegetation corresponds to the moss hummock type, intermixed with *Eriophorum vaginatum* and herbs such as *Rhododendron chamaemorus* (Figure 1d). A comparison of RGB orthomosaics derived from UAV data acquired at Stordalen Mire in July 2016 (3 cm resolution) and July 2022 (7 cm resolution) reveals that the degraded palsa site has transitioned toward greener vegetation and wetter conditions, both recognized indicators of ongoing permafrost degradation, while the palsa site exhibits relatively stable coloration (Figure S1) [69, 70].

2.2 | Sampling and Analyses

The field campaign was conducted between the end of the growing season and the beginning of the late shoulder season from September 20 to October 7, when soil temperatures remained above freezing (Figure S2a). The three sampling sites (palsa, intermediate, and degraded palsa) were selected based on the mean thaw depth measured within an area of two square meters with a minimum of 5 cm variation between the five measurements within the same location. Thaw depth was measured three times at each sampling site using a graduated steel rod of 145 cm in length. Thaw depth was measured every 3 days. Two soil profiles to 45 cm depth were described at the palsa site ($n = 2$) and to 60 cm depth at the intermediate site ($n = 2$). The soil profiles at palsa comprise a unique organic horizon. At intermediate, the organic layer constituted the first 25 cm followed by a transition layer of 15 cm thickness, then by a mineral layer [34, 64]. No soil profile was described at degraded palsa. SWC was monitored continuously using TEROS-12 capacitance sensors (METER Group, Pullman, WA, USA) probes with readings recorded every 10 min. At the palsa and the intermediate sites, the capacitance probes were installed at two depths (three probes at 10 cm and three probes at 30 cm). Since the degraded palsa site was waterlogged no capacitance probes were installed but measurements were collected four times at the soil surface using a portable capacitance probe. Redox potential was recorded at the intermediate site at two depths (redox probe ORP 30-1-BNC at 12.5 cm and redox probe ORP 30-1-B at 30 cm; SWAP instruments, Castricum, The Netherlands). A systematic recording of redox potential was performed at intervals of 30 min.

The topographic position index (TPI) of the study site is computed as the difference between the elevation of a focal cell and the mean elevation of its surrounding neighborhood within a digital elevation model (DEM):

$$\mathrm{TPI}\,(x,y) = z_{(x,y)} - \frac{1}{N}\sum_{i=1}^{N} z_i,$$

where $\mathrm{TPI}(x,y)$ = TPI value at cell coordinates (x,y), $z_{(x,y)}$ = elevation of the focal cell, z_i = elevation of neighboring cell i, N = number of surrounding cells in the rectangle window of 50×50 pixels [71]. Systematic vertical bias in a DEM, such as that introduced by UAV-based sensors, affects both the focal cell and its neighboring cells in a similar manner. As a result, local relative deviations in elevation remain detectable, allowing TPI to reliably capture landform positions such as ridges, valleys, and flat areas, even when absolute elevation values are subject to bias [72, 73]. The elevations of the palsa, intermediate, and degraded palsa sites were derived from a DEM generated through photogrammetry using RGB data from a drone survey conducted on September 21, 2021. The drone survey was executed on a cloudless day employing a DJI Mavic 2 Pro. A post-processing L1/L2 PPK (Post-Processed Kinematic) solution was applied using the SWEPOS network. A DEM and an orthomosaic were generated from the acquired data with a common spatial resolution of 0.6 cm. For accurate georeferencing of the DEM and the orthomosaic, six ground control points were collected with an Emlid Reach RS + GPS device.

Soil pore water was collected at the palsa, the intermediate, and the degraded palsa sites. Soil pore water was obtained using in situ rhizon samplers (Rhizosphere Research Products, Wageningen, The Netherlands, pore size of 0.2 μm) connected to 60 mL acid-washed syringes held under a vacuum with a wooden stick. Soil pore water was collected from the three locations (A, B, and C) per site as triplicates. At each location, soil pore water was collected at 10, 30, and 45 cm (palsa site, just above the permafrost table) or 60 cm depth (intermediate and degraded palsa sites) ($n = 9$ rhizon samplers per site). The sample collection was carried out between September 20 and October 7, 2021: the syringes were emptied once a day for three consecutive days into acid-washed polypropylene bottles and stored at 4°C. This results in a total of 161 soil pore water samples (54 soil pore water samples at the palsa and the degraded palsa sites and 53 at the intermediate site).

Soil pore waters were analyzed for pH and conductivity ($n = 54$ at the palsa and degraded palsa sites; $n = 53$ at the intermediate site), concentrations in DOC ($n = 53$ at the palsa and intermediate sites; $n = 54$ at the degraded palsa site), and cations and anions ($n = 51$ at the palsa site, $n = 53$ at the intermediate sites; $n = 54$ at the degraded palsa site). The priority for the chemical analyses was made on the measurement of the pH and conductivity then on the concentrations in DOC and finally on the concentrations in anions and cations explaining the difference in the number of measurements between the soil pore water analyses. The pH and conductivity were determined using a SevenCompact Duo S213 probe, while the DOC concentration was assessed using a TOC-L Analyzer (detection limit of 0.1 mg/L and accuracy of ±2%; Shimadzu, Kyoto, JP). Concentrations in major cations were quantified using optical emission spectrometer (ICP-OES, iCAP 6500 ThermoFisher Scientific, Waltham, MA, USA). The accuracy on major element concentrations (±7%, 4%, 3%, 4%, 4%, 2%, 4% for K, Na, Ca, Mg, Al, Fe, and Si, respectively) was assessed using the water reference material SLRS-4 [74]. The detection limits for major element concentrations (K, Na, Ca, Mg, Al, Fe, and Si) are 0.005, 0.001, 0.01,

10991530, 0, Downloaded from https://onlinelibrary.wiley.com/doi/10.1002/ppp.70018 by Université De Liège, Wiley Online Library on [27/11/2025]. See the Terms and Conditions (https://onlinelibrary.wiley.com/terms-and-conditions) on Wiley Online Library for rules of use; OA articles are governed by the applicable Creative Commons License

0.005, 0.01, 0.01, and 0.01 mg/L, respectively. Anion concentrations (SO_4^{2-}, Cl^-, NO_3^-) were determined using a Dionex IC20 ion chromatograph (ThermoFisher Scientific, Waltham, MA, USA) with a detection limit of 0.48, 0.47, and 0.68 mg/L, respectively. The accuracy for SO_4^{2-}, Cl^-, NO_3^- (±3%, 4%, and 4%, respectively) was assessed using river water certified reference material LGC6025, with a precision of ±2% for each anion.

2.3 | Geochemical Modeling

A geochemical modeling approach was used to predict to what extent Fe and DOC may be bound together in solution, and through which type of bond (complexation or sorption on precipitates).

First, the ratio of Fe^{2+} and ferric Fe^{3+} ions was predicted from the Fe concentration measured in the soil pore waters using the geochemical modeling program PHREEQC version 3 [75]. PHREEQC modeling was conducted on 10 soil pore water samples selected to represent a gradient in terms of depths (10 and 30 cm depth) and permafrost degradation (one profile from the palsa site [location B], each profile of the intermediate site [A, B, C], and one profile from the degraded palsa site [location C]). Each soil pore water constitutes one model run. The following parameters were used as input for the model for the 10 runs: Fe concentrations and measured field parameters (water pH, redox, and water temperature). For the redox potential, the following data were input into the model: (i) for the intermediate site, direct field measurements are available at two depths (12.5 and 30 cm); (ii) for the palsa site, the redox potential at 10 and 30 cm depth is assumed to be constant and the same as the redox potential measured at 12.5 cm depth at the intermediate site presenting similar SWC (Section 2.2); (iii) for the degraded palsa site, we used the redox potential measured in the Stordalen mire in degraded palsa sites with similar vegetation, water content, and active layer depth [76]. We assume the redox potential to be constant between 10 and 30 cm depth at the degraded palsa site, since the degraded palsa site is saturated with water, and since the redox potential is directly linked to the water saturation state of the soil [8, 77–79].

Then, the Fe speciation (Fe^{2+}/Fe^{3+} ratio) computed using PHREEQC was used in the geochemical modeling program Visual MINTEQ (version 3.1, April 2023) in conjunction with the Stockholm Humic Model (SHM) to predict the proportion of Fe oxides precipitates (ferrihydrite), Fe^{3+}-DOC complexes, Fe^{2+}-DOC complexes, and dissolved inorganic Fe^{2+} or Fe^{3+} in the soil pore waters [80]. The presence of the redox couple Fe^{2+}/Fe^{3+} was specified in the parameters, allowing the software to adjust the ratio in function of the inputs (ion concentrations, pH, and Eh) [81]. Each soil pore water constitutes one model run. The following parameters were used as input for the model for the 10 runs: anion and cation concentrations, Fe^{2+} and Fe^{3+} concentrations, and the measured field parameters (pH, conductivity, and redox potential). The same redox potentials were used as the ones used as input in PHREEQC. The following outputs of iron are obtained from the Visual MINTEQ geochemical modeling: total precipitated, dissolved inorganic, and bound to dissolved organic matter (DOM). In this model, a portion of the total DOC is regarded as "active" DOC, which is available for binding with protons and metals. The ratio of "active" DOM to DOC was set to 1.6, with 65% of the DOC assumed to be fulvic acids, in alignment with typical values observed in Swedish stream waters [82].

2.4 | Statistical Analyses

Kruskal–Wallis tests were performed to assess if there is a significant difference between the three sites (palsa, intermediate, and degraded), the three depths (10, 30, and 45/60 cm), or the three profiles (A, B, and C) of a site, followed by a post hoc comparison Dunn's test using Python (v. 3.7). Significance of all statistical analyses was determined at the $\alpha = 0.05$ level. A Principal Component Analysis (PCA) was conducted using thaw depth, SWC, TPI, and pH and conductivity of the soil pore water using R 4.2.3.

3 | Results

3.1 | Gradient in Thaw Depth, Relative Elevation, and SWC

The three sampling sites (palsa, intermediate, and degraded palsa) exhibit a thaw depth gradient (Figure 2), with mean thaw depth over time (represented by the error bars) and the locations A, B, and C ranging from 49 cm at the palsa site to 87 cm at the intermediate site and exceeding 145 cm at the degraded palsa site. Mean thaw depth over time significantly varies among the palsa, intermediate, and degraded palsa sites ($p < 0.001$, $n = 63$), with the most variable thaw depth observed (σ) at the intermediate site across the three locations (A, B, and C) ($\sigma_{palsa} = 2$ cm, $\sigma_{intermediate} = 5$ cm, $\sigma_{degraded\ palsa} = 0$ cm). TPI values were significantly lower at the degraded palsa site (-0.05 ± 0.03) compared with the palsa site (0.10 ± 0.06; $p < 0.001$). SWC at the palsa site ($0.404 \pm 0.047\ m^3/m^3$) is significantly lower than that at the degraded palsa site ($0.646 \pm 0.008\ m^3/m^3$; $p < 0.001$). SWC at the intermediate site has values between the palsa site and degraded palsa site values. The intermediate site displays the highest variability between locations, ranging from $0.457\ m^3/m^3$ to $0.623\ m^3/m^3$. For all sites, there are minimal fluctuations in SWC within each site ($n = 9$) during the field campaign (Figure S2b).

3.2 | pH and Conductivity of the Soil Pore Water

At the palsa site, pH values measured on soil pore waters range from 3.7 to 4.7 for the three depths (10, 30, and 45 cm), with a mean pH value of 4.0 ± 0.2 ($n = 53$) (Figure 3a). In contrast, at the degraded palsa site, pH values range from 4.0 to 5.3, indicating a significantly higher mean value of 4.6 ± 0.3 than at the palsa site ($n = 54$; $p < 0.001$). At 10 cm depth, pH values at the intermediate site are comparable to those measured at the palsa site; however, with increasing depth, pH values rise by nearly two units, resulting in a mean value of 5.5 ± 0.3 at 60 cm depth ($n = 18$), exceeding the pH at the corresponding depth at the degraded palsa site (4.9 ± 0.3, $n = 18$). For the three sites, the intermediate site shows the highest dispersion of pH values among the three depths ($\sigma_{palsa} = 0.2$, $\sigma_{intermediate} = 0.8$, $\sigma_{degraded\ palsa} = 0.3$). Mean soil pore water conductivity increases from the palsa site ($56 \pm 19\ \mu S/cm$ [$n = 53$])

10991530, 0, Downloaded from https://onlinelibrary.wiley.com/doi/10.1002/ppp.70018 by Université De Liège, Wiley Online Library on [27/11/2025]. See the Terms and Conditions (https://onlinelibrary.wiley.com/terms-and-conditions) on Wiley Online Library for rules of use; OA articles are governed by the applicable Creative Commons License

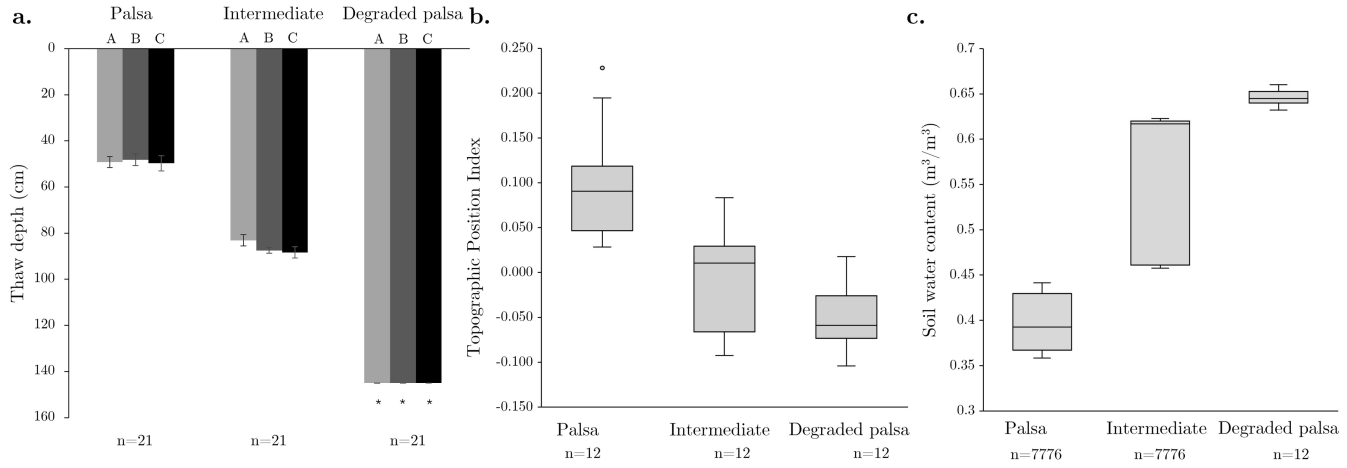

FIGURE 2 | Geophysical parameters measured during the field campaign at each sampling site (palsa, intermediate, and degraded palsa) between September 20 and October 7, 2021: (a) Mean thaw depths (cm) over time of locations A, B, and C taken every 3 days at the palsa ($n = 21$), intermediate ($n = 21$), and degraded palsa sites ($n = 21$; *: thaw depth > 145 cm), (b) topographic position index of the three locations (A, B, and C) computed from the DEM at each sampling site (palsa ($n = 12$), intermediate ($n = 12$), and degraded palsa ($n = 12$), where n is the number of pixels), and (c) Soil Water Content (m^3/m^3) measured with TDR probes every 5 min at 10 cm depth at the palsa ($n = 7776$) and intermediate sites ($n = 7776$), and measured three times on four occasions (27-09-21, 30-09-21, 04-10-21, and 07-10-21) at the degraded site ($n = 12$).

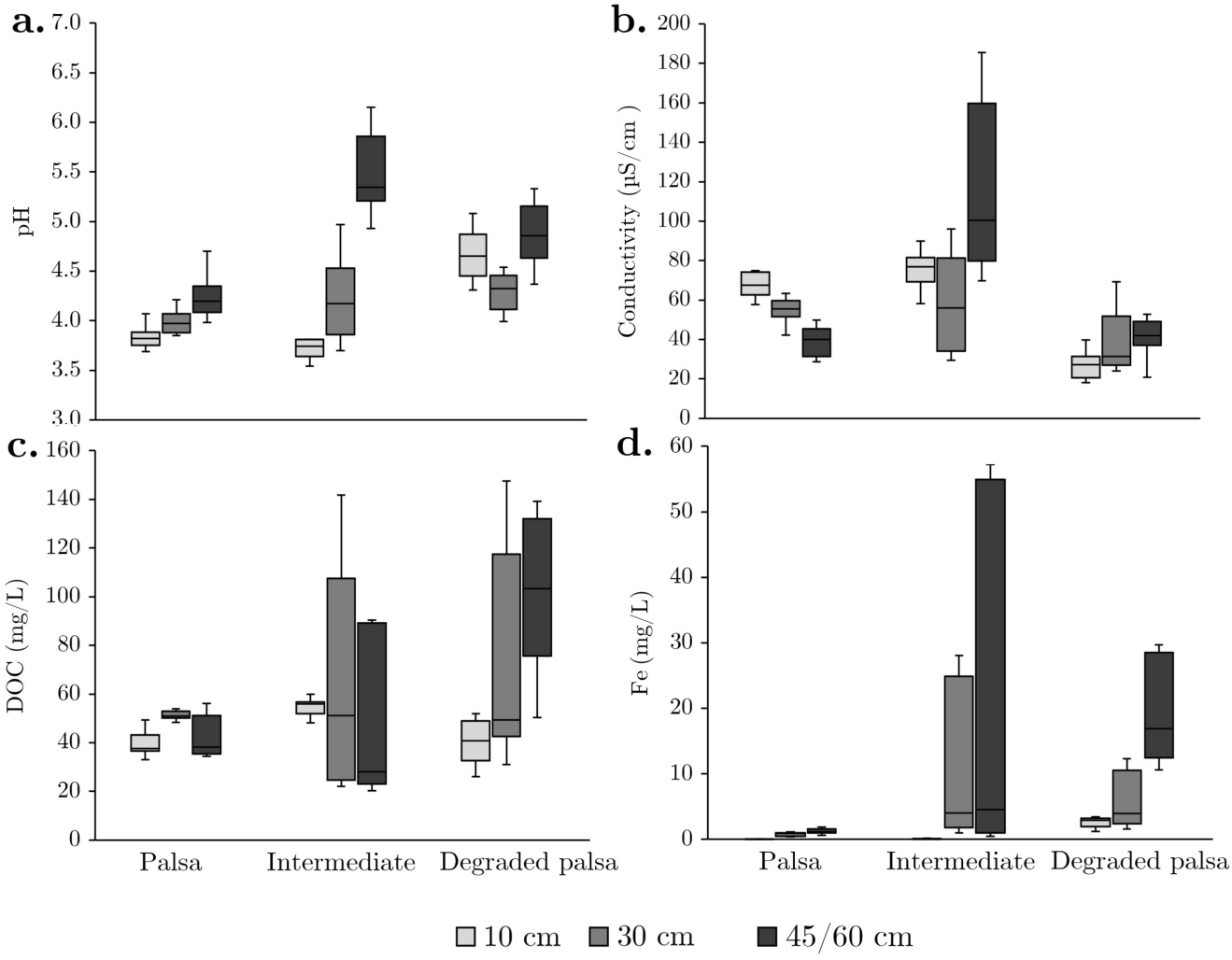

FIGURE 3 | (a) pH, (b) conductivity (µS/cm), (c) Fe concentration (mg/L), and (d) DOC concentration (mg/L) of the soil pore waters collected at the three sites (palsa [$n = 53$], intermediate [$n = 53$], and degraded palsa [$n = 54$]). Three depths were sampled between September 20 and October 7, 2021: at 10 cm depth for the three sites, at 30 cm for the three sites, and at 45 cm depth for the palsa site and 60 cm depth for the intermediate and degraded palsa sites.

10991530, 0, Downloaded from https://onlinelibrary.wiley.com/doi/10.1002/ppp.70018 by Université De Liège, Wiley Online Library on [27/11/2025]. See the Terms and Conditions (https://onlinelibrary.wiley.com/terms-and-conditions) on Wiley Online Library for rules of use; OA articles are governed by the applicable Creative Commons License

to the intermediate site ($83 \pm 36\,\mu S/cm$ [$n = 53$]) and decreases from the intermediate site to the degraded palsa site ($36 \pm 12\,\mu S/cm$ [$n = 54$]; Figure 3b). At the palsa site, conductivity decreases from 10 cm depth (mean value of $73 \pm 19\,\mu S/cm$, $n = 17$) to 45 cm depth ($39 \pm 7\,\mu S/cm$, $n = 18$). This decrease in conductivity with depth at the palsa site is inversely proportional to the pH trend with depth. Conversely, at the degraded palsa site, conductivity values exhibit no significant differences among the three depths ($p > 0.05$). The intermediate site displays the highest dispersion in conductivity values between locations (A, B, and C) ($\sigma_{palsa} = 19\,\mu S/cm$, $\sigma_{intermediate} = 36\,\mu S/cm$, $\sigma_{degraded\ palsa} = 12\,\mu S/cm$). At the intermediate site, in the transition layer from 30 to 60 cm depth, pore water conductivity increases from 59 ± 22 to $114 \pm 39\,\mu S/cm$, corresponding to a 1.3 unit pH increase between the same depths. Overall, for pH and conductivity values, the pH increases from the palsa site to the degraded palsa site, while it is highly variable at the intermediate site whereas the conductivity decreases from the palsa site to the degraded palsa site, but the electrical conductivity of soil pore water is highly variable at the intermediate site. At the surface of the intermediate site (10 cm depth), pH and conductivity values of soil pore waters are similar to the palsa site values. This similarity in values occurs at a depth where the permafrost is not degraded. In contrast, at depth (45 cm for palsa and 60 cm for intermediate), the pH and conductivity values at the intermediate site exceed those at the palsa site.

A Principal Component Analysis (PCA) including the five parameters presented in Sections 3.1 and 3.2 highlights that the first two principal components account for 83.1% of the total variance in the dataset (Figure 4a). TPI is negatively correlated with thaw depth (TD) and SWC, consistent with the observation that permafrost thaw leads to soil collapse and increased soil wetness. The variability associated with pH and conductivity in soil pore water is captured by the second principal component. The differentiation in geochemical conditions between palsa, intermediate, and degraded palsa sites is therefore revealed by three well-defined groups on the individuals' factor map (Figure 4b).

3.3 | DOC and Iron Concentrations in Soil Pore Water

In soil pore waters from the palsa, intermediate, and degraded palsa sites, the highest mean DOC concentrations occur at the intermediate site for all investigated depths (Figure 3c). The iron concentrations in soil pore water from the palsa site are lower than at the intermediate site and range from 0.01 to 2.84 mg/L with small variability relative to Fe across depths ($\sigma_{10\ cm} = 0.01$ mg/L, $\sigma_{30\ cm} = 0.39$ mg/L, $\sigma_{45\ cm} = 0.59$ mg/L; Figure 3d). Iron concentrations in soil pore water at the intermediate site range from 0.01 to 76.84 mg/L displaying extreme variability with depth ($\sigma_{10\ cm} = 0.04$ mg/L, $\sigma_{30\ cm} = 6.97$ mg/L, $\sigma_{60\ cm} = 32.88$ mg/L; Figure 3d). At the degraded palsa site, DOC and Fe concentrations in soil pore water increase with depth and show the largest variability in concentrations (Figure 3d).

Between locations A, B, and C, DOC concentrations in soil pore water were similar at 10 cm at each site (palsa site 3.83 ± 0.09 mg/L, intermediate site 56.36 ± 4.46 mg/L, and degraded palsa site 40.06 ± 8.06 mg/L; Figure 5). While DOC and Fe concentrations in soil pore water at the palsa site show little variations with depth (DOC: $\sigma_{10\ cm} = 5.96$ mg/L, $\sigma_{30\ cm} = 1.60$ mg/L, $\sigma_{45\ cm} = 7.44$ mg/L; Fe: $\sigma_{10\ cm} = 0.01$ mg/L, $\sigma_{30\ cm} = 0.40$ mg/L, $\sigma_{45\ cm} = 0.59$ mg/L), distinct trends emerge with depth at the intermediate and degraded palsa sites. At the intermediate site,

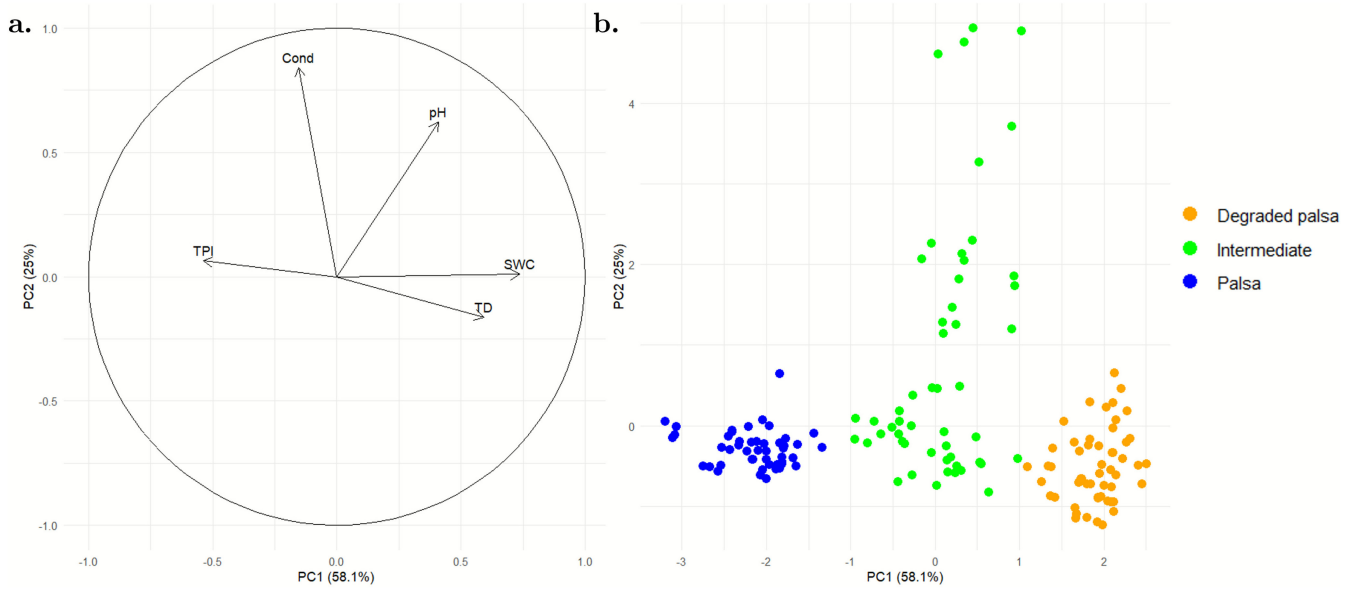

FIGURE 4 | Principal component analysis (PCA) results illustrating the relationships among environmental variables and sampling locations. (a) Correlation circle depicting the first two principal components, with axes labeled by their respective explained variance (%). Variables included are thaw depth (TD), soil water content (SWC), topographic position index (TPI), pH, and conductivity (Cond) of the soil pore waters. (b) Individuals factor map displaying sampling points color-coded by site type: blue for palsa, green for intermediate, and orange for degraded palsa, highlighting the distribution and clustering patterns of different site types with the analyzed variables. [Colour figure can be viewed at wileyonlinelibrary.com]

10991530, 0, Downloaded from https://onlinelibrary.wiley.com/doi/10.1002/ppp.70018 by Université De Liège, Wiley Online Library on [27/11/2025]. See the Terms and Conditions (https://onlinelibrary.wiley.com/terms-and-conditions) on Wiley Online Library for rules of use; OA articles are governed by the applicable Creative Commons License

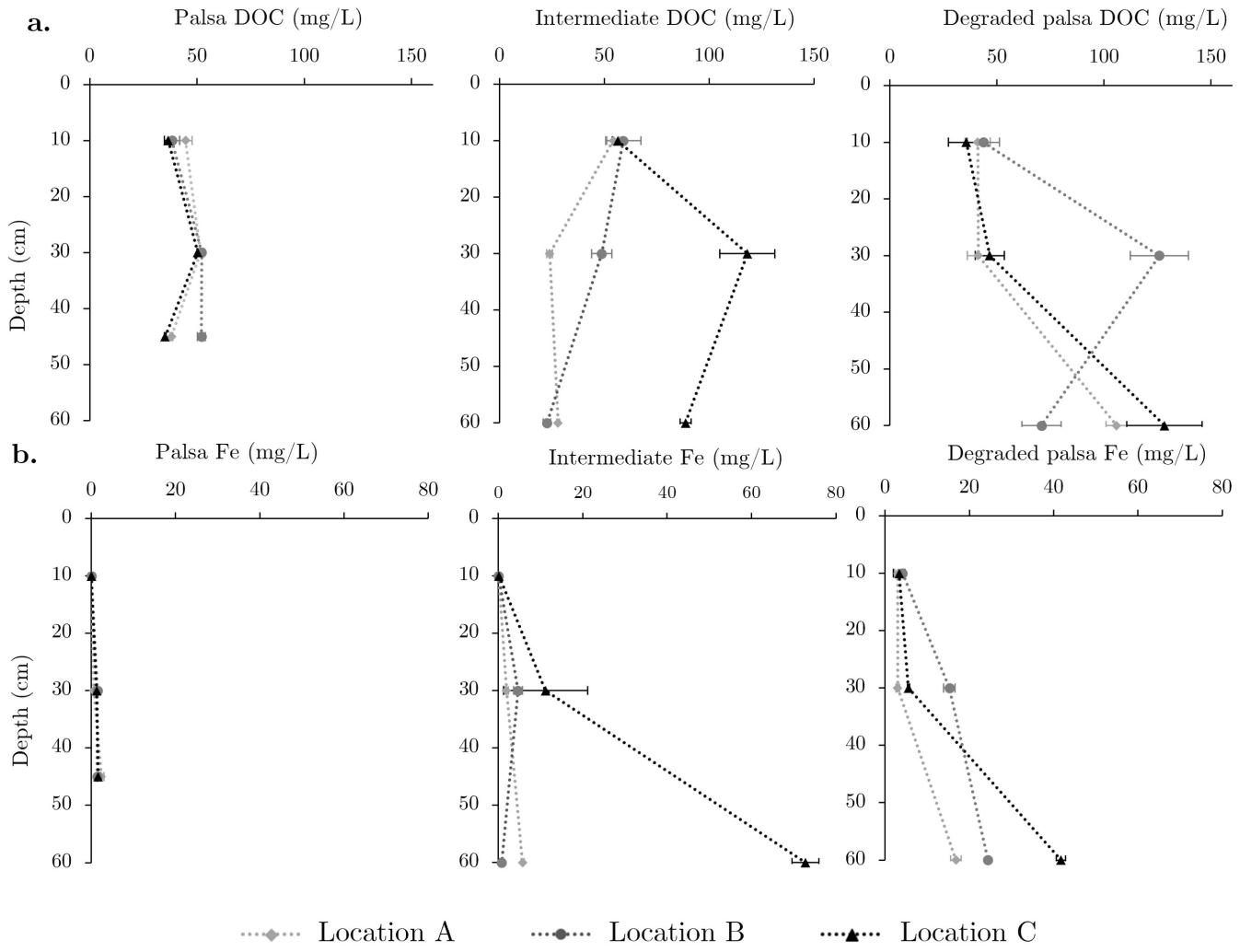

FIGURE 5 | Mean concentrations of (a) DOC (mg/L) and (b) Fe (mg/L) with depth measured from the soil pore water collected at the three locations (A [light gray diamonds], B [dark gray rounds], and C [black triangles]) at each site: palsa (10, 30, and 45 cm depth), intermediate, and degraded palsa (10, 30, and 60 cm depth) between September 20 and October 7, 2021. The error bars account for the data dispersion between the sampling dates.

location A exhibits a rapid decline of DOC concentrations from 54.20 ± 2.94 mg/L at 10 cm to 23.83 ± 1.29 mg/L at 30 cm, leveling off at 60 cm (27.87 ± 0.64 mg/L). Conversely, location C shows an opposing trend, registering almost double the DOC concentration in soil pore water at 30 cm (118.22 ± 13.10 mg/L) compared with 10 cm (56.31 ± 2.5 mg/L). As for DOC concentrations in soil pore water, location C consistently displays higher Fe concentrations compared with locations A and B. At the degraded palsa site, DOC concentrations in soil pore water present similar patterns with depth for locations A and C. Only location B shows a higher DOC concentration in soil pore water at 30 cm depth (125.75 ± 13.60) compared with location A (41.19 ± 5.04 mg/L) and C (46.61 ± 6.72 mg/L; $n = 6$). Variability in Fe concentrations in soil pore water among locations increases with depth ($\sigma_{10\ cm} = 1.05$ mg/L, $\sigma_{30\ cm} = 5.34$ mg/L, $\sigma_{60\ cm} = 27.67$ mg/L).

Overall, the thaw depth, the relative elevation (TPI), and the parameters measured on the soil pore waters (pH, conductivity, DOC, and Fe concentrations) are relatively constant for the palsa site. The palsa site represents the geochemical conditions of Stordalen soils where permafrost is poorly degraded. As the variability among those parameters is the largest for the intermediate site, that is, the site where permafrost is thawing (Figure 2a), the subsequent sections of the article will focus on the permafrost degradation process by comparing the intermediate site to the palsa site, which is defined as a reference site for poorly degraded permafrost soil.

3.4 | Geochemical Modeling of Iron Forms Concentrations in Soil Solutions

The PHREEQC model predicts that iron in the soil solutions of all locations is mainly in the form of Fe^{2+} (between 99% and 100%; Table S1) given the physicochemical conditions (acidic pH, ranging from 3.73 to 4.97) and reductive conditions (ranging from −116.46 to +174.22 mV).

We observed from the Visual MINTEQ model output that Fe^{3+} in soil pore water exists exclusively in the form of complexes with DOC (Figure 6). At a depth of 10 cm, the proportions of Fe^{2+} complexed to DOC in soil pore water varied significantly across sites, ranging from 24% (degraded palsa site) to 57%

10991530, 0, Downloaded from https://onlinelibrary.wiley.com/doi/10.1002/ppp.70018 by Université De Liège, Wiley Online Library on [27/11/2025]. See the Terms and Conditions (https://onlinelibrary.wiley.com/terms-and-conditions) on Wiley Online Library for rules of use; OA articles are governed by the applicable Creative Commons License

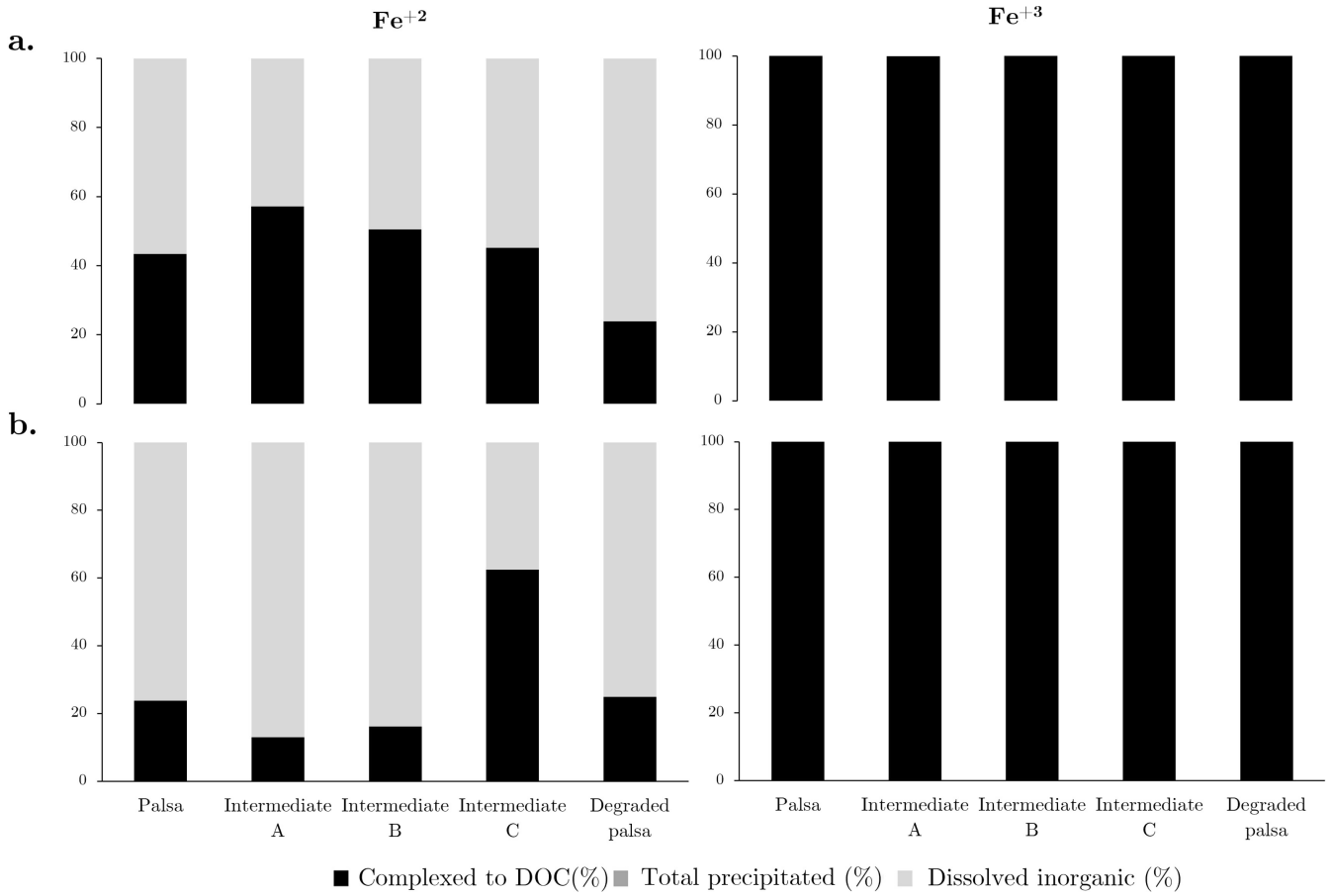

FIGURE 6 | Geochemical modeling output using Visual MINTEQ showing the proportions of iron complexed to organic carbon (black), precipitated (dark gray; absent), and dissolved inorganic (light gray) within soil solutions of one location at palsa, three locations at intermediate (A, B, and C), and one location at degraded palsa sites at (a) 10 and (b) 30 cm depth.

(intermediate A site), with the remainder of Fe^{2+} present in dissolved inorganic form. At 30 cm depth, the proportion of Fe^{2+} complexed to DOC in soil pore water decreases relative to 10 cm depth, except for intermediate C, where an increase of 17% is noted, and for the degraded palsa site, which maintained similar proportions of Fe^{2+} complexed to DOC in soil pore water relative to 10 cm depth (Figure 6b).

4 | Discussion

4.1 | Differentiating the Key Stages of Permafrost Degradation at the Submeter Scale

The three geophysical parameters (thaw depth, TPI, and SWC; Figure 2) show contrasting values between the two end-members of the gradient, that is, palsa and degraded palsa, and can be used to define the two end-member stages of permafrost degradation at Stordalen. These data are supported by the change in vegetation species between the two end-members where the palsa sampling site is largely composed of lichens and dwarf shrubs (e.g., *Betula nana*), while degraded palsa is mostly composed of *Sphagnum* mosses and tall graminoïds such as *Eriophorum vaginatum* [19, 22, 23, 27]. In contrast, we show that these geophysical parameters alone cannot be used to define the intermediate stage of permafrost thaw at Stordalen. Vegetation species are not a better parameter to differentiate the intermediate sites. Indeed, vegetation species at the intermediate site were mostly similar to species at the palsa site (Figure 1c,d), but vegetation species characteristic of degraded palsa sites were also present such as *Eriophorum* and mosses (Figure 1d,e). The three geophysical parameters and vegetation species are not sufficient to identify the intermediate stage of permafrost thaw [17] and this motivates a combination of geochemical parameters (soil pore water pH and conductivity; Figure 3). For these geochemical parameters, the intermediate site shows a larger variability in soil pore water pH and conductivity than the palsa and degraded palsa sites (highest dispersion in pH and conductivity values; Section 3.2).

By integrating variables such as TPI, thaw depth, SWC, soil pore water pH, and soil pore water conductivity, the PCA effectively differentiates between the various degradation stages of permafrost (Figure 4). These parameters can be used in combination and in addition to changes in vegetation species or other physical parameters such as temperature [21] to detect the transition between a palsa and thawed permafrost soil. This is important when seeking to identify submeter scale permafrost degradation when thaw depth is increasing but vegetation remains unchanged.

10991530, 0, Downloaded from https://onlinelibrary.wiley.com/doi/10.1002/ppp.70018 by Université De Liège, Wiley Online Library on [27/11/2025]. See the Terms and Conditions (https://onlinelibrary.wiley.com/terms-and-conditions) on Wiley Online Library for rules of use; OA articles are governed by the applicable Creative Commons License

4.2 | Submeter Scale Variability of Permafrost Thaw Controls Iron and Organic Carbon Release From Soil to Soil Pore Water

The high variability at the submeter scale of both pH and electrical conductivity values of the soil pore waters at the intermediate site compared with the palsa site (Figure 3a,b) can be explained by the degradation process of the permafrost and its consequences on soil hydrology. When permafrost is degrading, the reduction of pore space associated with ice melt causes the deformation of the ground surface resulting in the collapse of the soil surface. This subsidence has a significant impact on soil hydrology, given that the collapse of the soil surface brings the water table closer to the surface compared with soils where permafrost is intact [8, 83]. At the intermediate site, permafrost remains, acting as a hydrological barrier by preserving the disconnection between surface fluxes and the underlying groundwater. As a result, soils at the intermediate site receive water from direct precipitation (snow/rain), similar to palsa soils, and from runoff originating from the palsa site [19, 24, 26, 84]. Soils at the intermediate site have a larger depth to the permafrost table compared with the palsa site resulting in a greater water storage capacity in the soil column above the permafrost table. Additionally, bulk density in peatland soils generally increases with depth, which, in turn, reduces hydraulic conductivity [85–87]. Hence, water residence time is extended in these deeper soil horizons. This contrast in water storage capacity and hydraulic conductivity between the intermediate site and the palsa site is corroborated by the higher SWC at the intermediate site compared with the palsa site throughout the sampling period (Figure S2b). Furthermore, soil profiles at the palsa site only contained an organic horizon whereas soil profiles at the intermediate site showed a transition layer between organic and mineral horizons at 25 cm depth. Hence, permafrost thaw at the intermediate site has exposed a mineral-rich layer. The increase in SWC and the exposure of mineral-rich soils drive the increase in pH at the intermediate site. This is because the high SWC at 30 cm depth allows for the weathering of newly exposed minerals releasing cations in the soil pore water at the intermediate site, which consumes protons and hence increases the pH [33]. This is in line with the fact that in Arctic peatlands, higher SWC tends to increase pH by promoting ion mobility and cation leaching, while lower SWC is linked to more acidic conditions [33, 38]. Mineral weathering is facilitated by the high SWC in peatland soils and prolonged water residence times, resulting from the combination of high water retention capacity and low hydraulic conductivity [85, 88]. This contributes to explaining the large range of soil pore water pH and conductivity values at intermediate sites compared with palsa and degraded palsa sites.

To explain the submeter scale variability of soil pore water pH and conductivity values between the three locations (A, B, and C) at the intermediate site (Figure 3a,b), we consider the distance to the permafrost table to compare the soil pore water samples from the intermediate site to those from the palsa site used as a reference. For the pH, the three intermediate profiles follow the same trend along the soil profile (Figure 7a): lower values in the surface similar to the pH values at the palsa site, then an increase of almost two pH units with depth, with a larger pH increase in location C than in location B, and in location B than in location A. From the thaw depth measurements collected at the three locations, there is evidence of a micro-scale permafrost degradation gradient with location C presenting a deeper permafrost than location B, and location B a deeper permafrost than location A (Figure 2a). This supports that the increase in soil pore water pH at depth among the three profiles from the intermediate site can be explained by the degree of degradation of the permafrost [25, 26, 76]. The more degraded the permafrost, the more mineral-rich the unfrozen soil horizon. Weathering of these newly exposed minerals allows for cation release into the soil pore water: This is supported by the higher soil pore water conductivity at depth in location C than in location B, and in location B than in location A (Figure 7b). With these data, we demonstrate that a slight change in thaw depth (e.g., on a cm scale) in the degradation results in resolvable changes in the physicochemical conditions of the soil pore water. We demonstrate that these resolvable changes can be used to identify the key intermediate state representing a transition between palsa and degraded palsa.

Permafrost degradation has resulted in resolvable changes in soil pore water chemistry at depth between palsa and intermediate sites. We measured systematically higher concentrations of Fe in soil pore water at 30 and 60 cm depth at intermediate-location C compared with the palsa site (Figure 7d). It is also at intermediate-location C that the higher DOC concentrations in soil pore waters are measured relative to the palsa site, with the highest DOC concentrations at 30 cm depth (Figure 7c). The increase in Fe and DOC concentrations in soil pore waters from intermediate-location C compared with the palsa can be explained by the changing hydrological conditions resulting from permafrost thaw and its consequences on the soil redox potential. The SWC is known to dictate the soil redox potential [8, 38, 77, 79, 89, 90]. This is supported by field data of SWC (at 10 and 30 cm; Figure S2b) and soil redox potential (at 12.5 and 30 cm; Figure S3) at the intermediate site. At 10 cm where the SWC is lower (Figure S2b), intermediate soils show oxic conditions (mean value of +174.22 mV) whereas, at 30 cm depth where the SWC is higher, the redox potential is lower (mean value of −116.46 mV; Figure S3).

The higher SWC at the intermediate site relative to the palsa site (Figure 2c) lowers the redox potential, which favors Fe oxide dissolution and thereby increases the Fe concentration in soil pore water [51]. The higher Fe concentrations at 30 and 60 cm correspond to soil horizons containing a higher proportion of poorly crystalline Fe oxides in soils in the transition layer between organic and mineral soil horizons and in the mineral layer (corresponding to the layer at 30 and 60 cm depth, respectively) relative to the organic layer (corresponding to the layer at 10 cm depth) [34]. The higher proportion of poorly crystalline Fe oxides in these horizons results in part from the increase in pH in more mineral-rich soils (Figure 7a,d, [51]). Together, the higher soil pore water Fe concentrations at 30 and 60 cm point to a key location for soil to soil pore water Fe transfer upon increasing SWC (and shifting Eh). This is in line with our findings demonstrating that iron in these soil environments is predominantly as Fe^{2+} (Section 3.4). Increased SWC influences the capacity of Fe^{2+} to form complexes with DOC, as supported by the decrease in the proportion of Fe^{2+}-DOC complexes between 10 cm and 30 cm depth at the palsa, intermediate A, and intermediate B sites (Figure 6a,b). This trend is likely due to the dilution effect, where increased water content lowers the concentration of Fe^{2+}, reducing the likelihood of forming complexes with DOC. However, at intermediate C, the higher Fe^{2+} concentrations

10991530, 0, Downloaded from https://onlinelibrary.wiley.com/doi/10.1002/ppp.70018 by Université De Liège, Wiley Online Library on [27/11/2025]. See the Terms and Conditions (https://onlinelibrary.wiley.com/terms-and-conditions) on Wiley Online Library for rules of use; OA articles are governed by the applicable Creative Commons License

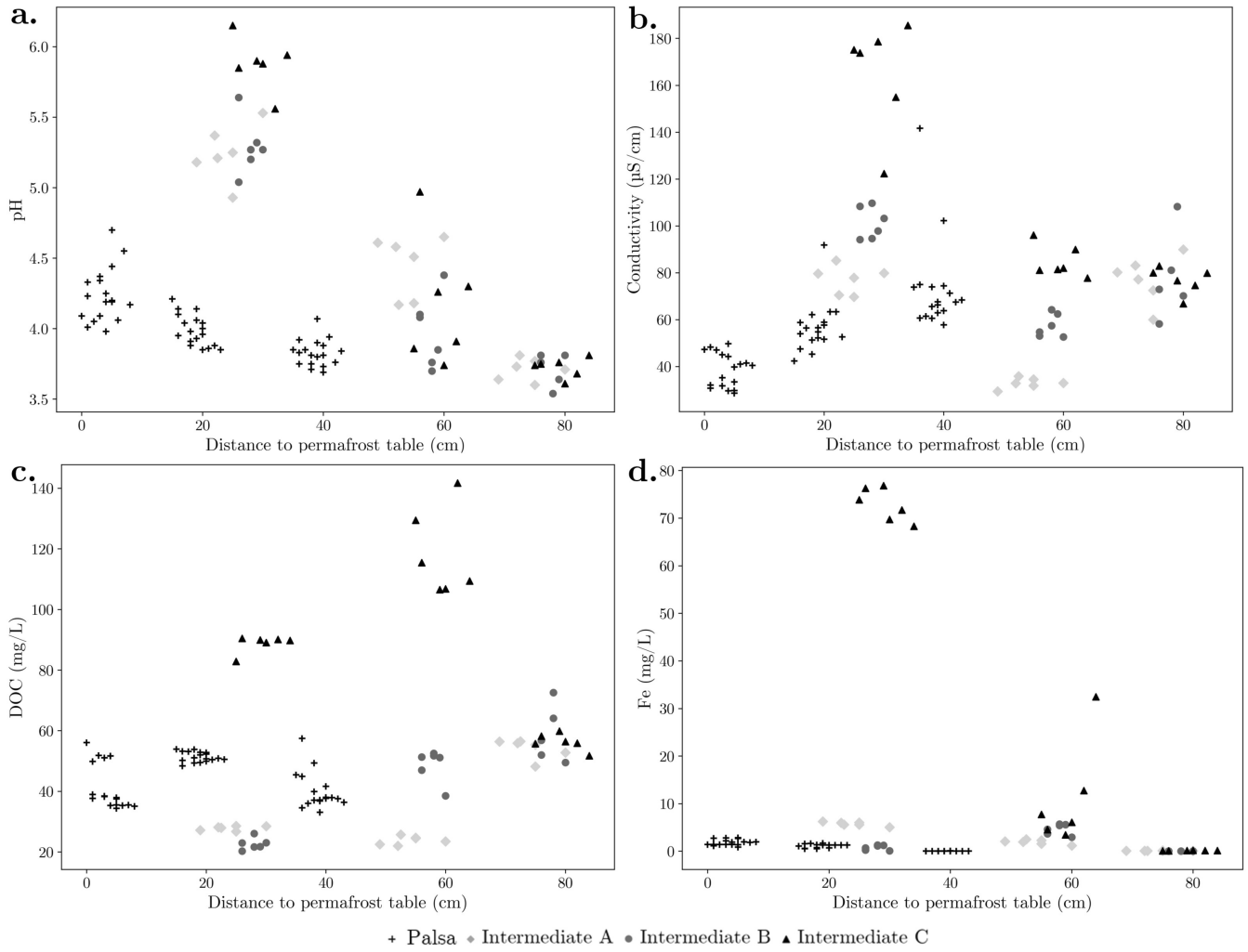

FIGURE 7 | Physicochemical parameters ((a) pH and (b) conductivity [µS/cm]) and (c) DOC (mg/L) and (d) Fe (mg/L) concentrations measured from the soil pore waters collected at the three locations at palsa (black cross; $n = 53$) used as reference and at location A (light gray diamond; $n = 18$), location B (dark gray circle, $n = 18$), and location C (black triangle, $n = 18$) of intermediate. Values are plotted against the distance to the permafrost table (cm) meaning that values close to the X-axis are values measured on pore waters collected just above the permafrost table and values at the top of the graphs are measurements made on soil pore waters that were collected closer to the surface.

result in increased Fe^{2+}-DOC complex proportions at 30 cm depth, indicating that elevated Fe^{2+} levels promote DOC stabilization through complex formation even under higher soil moisture conditions. In contrast, the degraded palsa site shows no change in the proportion of Fe^{2+}-DOC complexes or in SWC, as the entire soil profile is waterlogged. However, the Fe^{2+}/Fe^{3+} ratio is strongly linked to the Eh-pH conditions. Chauhan et al. [62] have demonstrated that thaw ponds in the bog region of Stordalen mire, corresponding to the degraded palsa site in this study, constitute major hotspots for organic carbon and iron accumulation. Since these ponds are exposed to the atmosphere, the water tends to become oxic, which shifts the ratio of iron speciation from being dominated by Fe^{2+} toward a balance between the two forms. Combining this knowledge with our results sheds light on the potential for the DOC to be stabilized through association with Fe^{2+} and Fe^{3+} as soon as the soil pore water reaches the surface. This could mean that a large proportion of DOC in the soil pore water at the degraded palsa site could be less vulnerable to microbial decomposition. We show that submeter scale variations in permafrost thaw depth and SWC change the conditions in pH and redox potential [91, 92], and thereby change the Fe and DOC concentrations in soil pore water and their capacity to form Fe-DOC complexes.

4.3 | Fate of DOC Along the Soil–River Continuum

Hydrological pathways and water residence times modulate the amount of Fe and its association with DOC in Arctic rivers [93, 94]. To what extent soil to soil pore water iron supply modulates aquatic DOC fate remains uncertain [59, 63]. Toward this aim, our findings align with the broader understanding that the permafrost degradation continuum extends beyond the degraded palsa, continuing toward river systems, as described by Olefeldt and Roulet [26]. This continuum facilitates the lateral flow of DOC from the peatland into adjacent rivers, driven by the movement of soil pore water. As this water is transported into the river system, it encounters new physicochemical conditions. For instance, Hirst et al. [93] observed that in an Arctic river in interior Alaska, pH levels could increase up to 7 within the same season,

10991530, 0, Downloaded from https://onlinelibrary.wiley.com/doi/10.1002/ppp.70018 by Université De Liège, Wiley Online Library on [27/11/2025]. See the Terms and Conditions (https://onlinelibrary.wiley.com/terms-and-conditions) on Wiley Online Library for rules of use; OA articles are governed by the applicable Creative Commons License

creating an environment where Fe speciation changes substantially. The increase in pH is probably due to the inflow of more neutral to slightly alkaline groundwater containing bicarbonate, which is particularly noticeable in large Arctic rivers (e.g., Lena River or Mackenzie River) due to their stronger connection to deep groundwater reservoirs [95–98]. These shifts in pH and redox conditions significantly influence Fe-DOC interactions, altering the stability and form of Fe complexes. Using a geochemical modeling approach similar to the one used for the palsa to degraded palsa gradient (combining PHREEQC for Fe^{2+}, Fe^{3+}, and Visual MINTEQ for Fe association to DOC), we simulated the changing geochemical conditions for Fe-DOC complexes exported from soil to rivers. We used the Fe and DOC concentrations in soil pore water from the degraded palsa site (Figure 3c,d), and we set up conditions for Arctic rivers with the pH at 7 [93, 99–101] and the redox potential at +600 mV [90, 102]. Under these conditions, Fe^{2+} is nearly entirely oxidized to Fe^{3+} (99%, Table S1), and subsequently precipitates as poorly crystalline iron oxides (Figure 8). This transformation reduces the solubility of Fe and the formation of Fe-DOC complexes. This suggests that Fe-DOC complexes formed in permafrost peatland soils are likely destabilized in the river. The released Fe can then form new ferrihydrite precipitates (e.g., [103]) and a new surface on which DOC can attach or low molecular weight complexes with DOC [59].

Whether DOC is bound to the surface of ferrihydrite or transported as low molecular weight Fe-DOC complexes, could impact microbial, and photochemical degradation of DOC in rivers [104, 105]. Notably, microbial degradation favors smaller molecules of DOC (e.g., aliphatics; [106]) whereas photodegradation targets larger molecules of DOC (e.g., aromatics; [107]). Once bound to DOC, it is considered that Fe promotes the photodegradation of larger aromatic molecules [63] and can catalyze microbial degradation of smaller DOC molecules (e.g., [108]). In this study, we show that permafrost degradation along a palsa to degraded palsa gradient controls the supply of Fe-DOC complexes (mainly as Fe^{2+}-DOC complexes) released from soils to aquatic bodies. The amount of Fe transported is driven by water table fluctuation following e.g., summer rain. Our modeled scenarios (Figure 8) support that exposing these Fe-DOC complexes to more oxic conditions and higher pH along the soil to river continuum contributes to destabilize the Fe-DOC complexes and favors the formation of poorly crystalline Fe oxides (ferrihydrite) which can adsorb DOC [46, 47, 55–57]. From this, we show that the stage of permafrost degradation modulates the amount and oxidation state of Fe bound to DOC that is transported from soil to soil pore water, and in turn, how much Fe will be available to modulate DOC fate in aquatic systems.

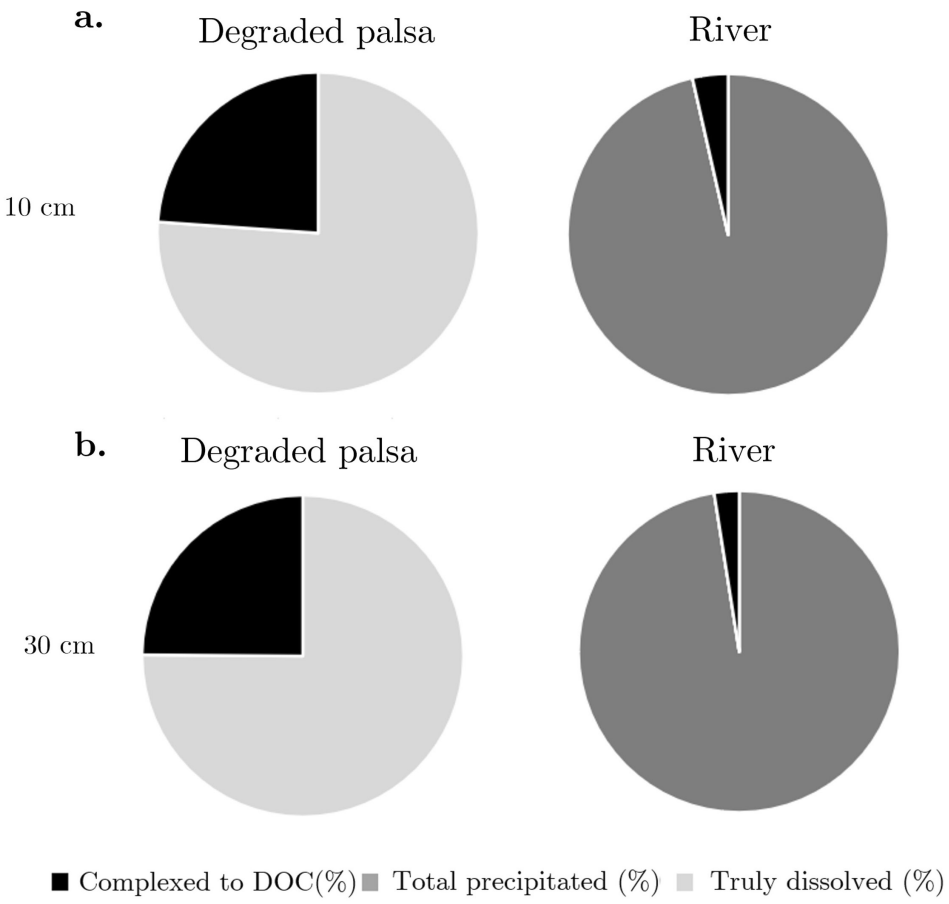

FIGURE 8 | Proportions of the three types of Fe form (complexed with DOC [black], precipitated [dark gray], and dissolved inorganic [light gray]) computed from the concentrations of Fe and DOC measured from the soil solutions collected at the degraded palsa site at (a) 10 and (b) 30 cm depth using two geochemical models (PHREEQC and Visual MINTEQ). Fe at the degraded palsa site is 99% as Fe^{2+}, while at river, it is mainly composed of Fe^{3+} (99%).

10991530, 0, Downloaded from https://onlinelibrary.wiley.com/doi/10.1002/ppp.70018 by Université De Liège, Wiley Online Library on [27/11/2025]. See the Terms and Conditions (https://onlinelibrary.wiley.com/terms-and-conditions) on Wiley Online Library for rules of use; OA articles are governed by the applicable Creative Commons License

5 | Conclusion

Our study on permafrost peatland for Stordalen, Abisko, Sweden leads to the following main outcomes:

1. Combining variables such as relative elevation (TPI), thaw depth, SWC, soil pore water pH, and soil pore water conductivity to changes in vegetation species effectively differentiates submeter scale permafrost degradation and allows the detection of the transition between a palsa and thawed permafrost soil.
2. Submeter scale variations in permafrost thaw depth and SWC change the soil geochemical conditions (pH and redox potential), and thereby drive the Fe and DOC release in soil pore water and the capacity to form Fe-DOC complexes.
3. Distinct proportions of Fe^{2+}-DOC complexes are exported from soil as a function of their stage of permafrost degradation, and the fate of these Fe-DOC complexes is likely to evolve along the soil to river continuum according to geochemical modeled scenarios.

This study highlights the need to consider the range of associations between Fe and DOC released from permafrost degradation to rivers to better quantify the availability of DOC for microbial degradation.

Acknowledgments

We extend our gratitude to the Swedish Polar Research Secretariat and SITES for their support of the research conducted at the Abisko Scientific Research Station. SITES is funded by the Swedish Research Council. The authors are grateful to 'Länsstyrelsen Norrbotten' for allowing this scientific research in the Stordalens naturreservat. Acknowledgment is given to the analytical platform MOCA at UCLouvain, as well as to A. Monhonval and E. Mauclet for their assistance with field sampling. This work is an Action de Recherche Concertée (ARC), no. 21/26–119, funded by the Fédération Wallonie-Bruxelles (FWB). This work received funding from the European Research Council (ERC) under the Horizon 2020 research and innovation program (ERC Starting Grant, WeThaw, no. 714617) awarded to S.O., as well as from the Fonds National de la Recherche Scientifique (FNRS) supporting S. Opfergelt (FC69480), K. Van Oost, S. Lambot., M. Villani (FC49507), and E. du Bois d'Aische (FC54613).

Conflicts of Interest

The authors declare no conflicts of interest.

Data Availability Statement

The dataset is available on 10.14428/DVN/9F4TND.

References

1. G. Hugelius, J. Strauss, S. Zubrzycki, et al., "Estimated Stocks of Circumpolar Permafrost Carbon With Quantified Uncertainty Ranges and Identified Data Gaps," *Biogeosciences* 11, no. 23 (2014): 6573–6593, https://doi.org/10.5194/bg-11-6573-2014.

2. J. Strauss, M. Fuchs, G. Hugelius, et al., *Organic Matter Storage and Vulnerability in the Permafrost Domain* (Elsevier, 2024), https://doi.org/10.1016/B978-0-323-99931-1.00164-1.

3. E. A. G. Schuur, A. D. McGuire, C. Schädel, et al., "Climate Change and the Permafrost Carbon Feedback," *Nature* 520, no. 7546 (2015): 171–179, https://doi.org/10.1038/nature14338.

4. B. Fox-Kemper, H. T. Hewitt, C. Xiao, et al., "Ocean, Cryosphere, and Sea Level Change," in *Climate Change 2021: The Physical Science Basis. Contribution of Working Group I to the Sixth Assessment Report of the Intergovernmental Panel on Climate Change*, eds. V. Masson-Delmotte, P. Zhai, A. Pirani, et al. (Cambridge University Press, 2021).

5. T. Minayeva and A. Sirin "Wetlands-Threatened Arctic Ecosystems: Vulnerability to Climate Change and Adaptation Options," (2009): 76–83.

6. T. Minayeva, A. Sirin, P. Kershaw, and O. Bragg, "Arctic Peatlands," in *The Wetland Book*, eds. C. M. Finlayson, G. R. Milton, R. C. Prentice, and N. C. Davidson (Springer Netherlands, 2018), 275–288, https://doi.org/10.1007/978-94-007-4001-3_109.

7. S. C. Zoltai, C. Tarnocai, G. F. Mills, and H. Veldhuis "Wetlands of Subarctic Canada," (1988), http://cfs.nrcan.gc.ca/publications?id=19221.

8. C. G. Andresen, D. M. Lawrence, C. J. Wilson, et al., "Soil Moisture and Hydrology Projections of the Permafrost Region—A Model Intercomparison," *Cryosphere* 14, no. 2 (2020): 445–459, https://doi.org/10.5194/tc-14-445-2020.

9. E. J. Lundin, J. Klaminder, R. Giesler, et al., "Is the Subarctic Landscape Still a Carbon Sink? Evidence From a Detailed Catchment Balance," *Geophysical Research Letters* 43, no. 5 (2016): 1988–1995, https://doi.org/10.1002/2015GL066970.

10. D. Olefeldt, S. Goswami, G. Grosse, et al., "Circumpolar Distribution and Carbon Storage of Thermokarst Landscapes," *Nature Communications* 7, no. 1 (2016): 13043, https://doi.org/10.1038/ncomms13043.

11. C. Voigt, M. E. Marushchak, M. Mastepanov, et al., "Ecosystem Carbon Response of an Arctic Peatland to Simulated Permafrost Thaw," *Global Change Biology* 25, no. 5 (2019): 1746–1764, https://doi.org/10.1111/gcb.14574.

12. A. F. Borge, S. Westermann, I. Solheim, and B. Etzelmüller, "Strong Degradation of Palsas and Peat Plateaus in Northern Norway During the Last 60 Years," *Cryosphere* 11, no. 1 (2017): 1–16, https://doi.org/10.5194/tc-11-1-2017.

13. L. C. P. Martin, J. Nitzbon, J. Scheer, et al., "Lateral Thermokarst Patterns in Permafrost Peat Plateaus in Northern Norway," *Cryosphere* 15, no. 7 (2021): 3423–3442, https://doi.org/10.5194/tc-15-3423-2021.

14. C. Renette, M. Olvmo, S. Thorsson, B. Holmer, and H. Reese, *Multitemporal UAV LiDAR Detects Seasonal Heave and Subsidence on Palsas* (EGUsphere, 2024), 1–27, https://doi.org/10.5194/egusphere-2024-141.

15. K.-Y. Chang, W. Riley, P. Crill, R. F. Grant, V. Rich, and S. Saleska, "Large Carbon Cycle Sensitivities to Climate Across a Permafrost Thaw Gradient in Subarctic Sweden," *Cryosphere* 13 (2019): 647–663, https://doi.org/10.5194/tc-13-647-2019.

16. N. Malmer, T. Johansson, M. Olsrud, and T. R. Christensen, "Vegetation, Climatic Changes and Net Carbon Sequestration in a North-Scandinavian Subarctic Mire Over 30 Years," *Global Change Biology* 11, no. 11 (2005): 1895–1909, https://doi.org/10.1111/j.1365-2486.2005.01042.x.

17. M. S. Patzner, N. Kainz, E. Lundin, et al., "Seasonal Fluctuations in Iron Cycling in Thawing Permafrost Peatlands," *Environmental Science & Technology* 56, no. 7 (2022): 4620–4631, https://doi.org/10.1021/acs.est.1c06937.

18. J. van Huissteden, "The Role of Ground Ice," in *Thawing Permafrost: Permafrost Carbon in a Warming Arctic*, ed. J. van Huissteden (Springer International Publishing, 2020), 107–177, https://doi.org/10.1007/978-3-030-31379-1_3.

10991530, 0, Downloaded from https://onlinelibrary.wiley.com/doi/10.1002/ppp.70018 by Université De Liège, Wiley Online Library on [27/11/2025]. See the Terms and Conditions (https://onlinelibrary.wiley.com/terms-and-conditions) on Wiley Online Library for rules of use; OA articles are governed by the applicable Creative Commons License

19. K. Bäckstrand, P. M. Crill, M. Mastepanov, T. R. Christensen, and D. Bastviken, "Total Hydrocarbon Flux Dynamics at a Subarctic Mire in Northern Sweden," *Journal of Geophysical Research: Biogeosciences* 113, no. G3 (2008): 2008JG000703, https://doi.org/10.1029/2008JG000703.

20. M. Lupascu, J. L. Wadham, E. R. C. Hornibrook, and R. D. Pancost, "Methanogen Biomarkers in the Discontinuous Permafrost Zone of Stordalen, Sweden," *Permafrost and Periglacial Processes* 25, no. 4 (2014): 221–232, https://doi.org/10.1002/ppp.1823.

21. T. V. Raudina, S. V. Loiko, G. I. Istigechev, S. P. Kulizhskiy, L. Orgogozo, and O. S. Pokrovsky, "Contrasting Soil Temperature Regimes in Peatlands of the Discontinuous Permafrost Zone (Western Siberia)," *Geoderma* 457 (2025): 117294, https://doi.org/10.1016/j.geoderma.2025.117294.

22. J. Deng, C. Li, S. Frolking, Y. Zhang, K. Bäckstrand, and P. Crill, "Assessing Effects of Permafrost Thaw on C Fluxes Based on Multiyear Modeling Across a Permafrost Thaw Gradient at Stordalen, Sweden," *Biogeosciences* 11, no. 17 (2014): 4753–4770, https://doi.org/10.5194/bg-11-4753-2014.

23. M. Hough, A. McClure, B. Bolduc, et al., "Biotic and Environmental Drivers of Plant Microbiomes Across a Permafrost Thaw Gradient," *Frontiers in Microbiology* 11 (2020): 796, https://doi.org/10.3389/fmicb.2020.00796.

24. R. Lindsay, "Lagg fen," in *The Wetland Book*, eds. C. M. Finlayson, G. R. Milton, R. C. Prentice, and N. C. Davidson (Springer Netherlands, 2018a), 309–312, https://doi.org/10.1007/978-94-007-4001-3_257.

25. M. Lupascu, J. L. Wadham, E. R. C. Hornibrook, and R. D. Pancost, "Temperature Sensitivity of Methane Production in the Permafrost Active Layer at Stordalen, Sweden: A Comparison With Non-permafrost Northern Wetlands," *Arctic, Antarctic, and Alpine Research* 44, no. 4 (2012): 469–482.

26. D. Olefeldt and N. T. Roulet, "Effects of Permafrost and Hydrology on the Composition and Transport of Dissolved Organic Carbon in a Subarctic Peatland Complex," *Journal of Geophysical Research: Biogeosciences* 117, no. G1 (2012): 2011JG001819, https://doi.org/10.1029/2011JG001819.

27. R. K. Varner, P. M. Crill, S. Frolking, et al., "Permafrost Thaw Driven Changes in Hydrology and Vegetation Cover Increase Trace Gas Emissions and Climate Forcing in Stordalen Mire From 1970 to 2014," *Philosophical Transactions of the Royal Society A: Mathematical, Physical and Engineering Sciences* 380, no. 2215 (2021): 20210022, https://doi.org/10.1098/rsta.2021.0022.

28. M. Palace, C. Herrick, J. DelGreco, et al., "Determining Subarctic Peatland Vegetation Using an Unmanned Aerial System (UAS)," *Remote Sensing* 10, no. 9 (2018): 9, https://doi.org/10.3390/rs10091498.

29. S. Sjögersten, M. Ledger, M. Siewert, et al., "Optical and Radar Earth Observation Data for Upscaling Methane Emissions Linked to Permafrost Degradation in Sub-Arctic Peatlands in Northern Sweden," *Biogeosciences* 20 (2023): 4221–4239, https://doi.org/10.5194/bg-20-4221-2023.

30. T. V. Armentano, J. P. Sah, M. S. Ross, D. T. Jones, H. C. Cooley, and C. S. Smith, "Rapid Responses of Vegetation to Hydrological Changes in Taylor Slough, Everglades National Park, Florida, USA," *Hydrobiologia* 569, no. 1 (2006): 293–309, https://doi.org/10.1007/s10750-006-0138-8.

31. J.-C. Svenning and B. Sandel, "Disequilibrium Vegetation Dynamics Under Future Climate Change," *American Journal of Botany* 100, no. 7 (2013): 1266–1286, https://doi.org/10.3732/ajb.1200469.

32. C. Estop-Aragonés, D. Olefeldt, B. W. Abbott, et al., "Assessing the Potential for Mobilization of Old Soil Carbon After Permafrost Thaw: A Synthesis of ^{14}C Measurements From the Northern Permafrost Region," *Global Biogeochemical Cycles* 34, no. 9 (2020): e2020GB006672, https://doi.org/10.1029/2020GB006672.

33. E. Herndon, L. Kinsman-Costello, and S. Godsey, "Biogeochemical Cycling of Redox-Sensitive Elements in Permafrost-Affected Ecosystems," in *Biogeochemical Cycles: Ecological Drivers and Environmental Impact* (Scopus, 2020), 245–265, https://doi.org/10.1002/9781119413332.ch12.

34. M. S. Patzner, C. W. Mueller, M. Malusova, et al., "Iron Mineral Dissolution Releases Iron and Associated Organic Carbon During Permafrost Thaw," *Nature Communications* 11, no. 1 (2020): 6329, https://doi.org/10.1038/s41467-020-20102-6.

35. E. Gorham, J. A. Janssens, G. A. Wheeler, and P. H. Glaser, "The Natural and Anthropogenic Acidification of Peatlands," in *Effects of Atmospheric Pollutants on Forests, Wetlands and Agricultural Ecosystems*, ed. T. C. Hutchinson and K. M. Meema (Springer, 1987), 493–512, https://doi.org/10.1007/978-3-642-70874-9_36.

36. S. P. Manalu, T. Sabrina, and Y. A. Sari, "Exploring the Triad: PH, Nitrogen, and Phosphorus Characteristics of Peat Soils in Humbang Hasundutan Regency," *E3S Web of Conferences* 519 (2024): 03009, https://doi.org/10.1051/e3sconf/202451903009.

37. S. Robinson, M. Turetsky, and I. Kettles, "Permafrost and Peatland Carbon Sink Capacity With Increasing Latitude," (2003).

38. D. A. Lipson, D. Zona, T. K. Raab, F. Bozzolo, M. Mauritz, and W. C. Oechel, "Water-Table Height and Microtopography Control Biogeochemical Cycling in an Arctic Coastal Tundra Ecosystem," *Biogeosciences* 9, no. 1 (2012): 577–591, https://doi.org/10.5194/bg-9-577-2012.

39. T. Caruso, F. T. De Vries, R. D. Bardgett, and J. Lehmann, "Soil Organic Carbon Dynamics Matching Ecological Equilibrium Theory," *Ecology and Evolution* 8, no. 22 (2018): 11169–11178, https://doi.org/10.1002/ece3.4586.

40. G. Wang, W. Zhang, W. Sun, T. Li, and P. Han, "Modeling Soil Organic Carbon Dynamics and Their Driving Factors in the Main Global Cereal Cropping Systems," *Atmospheric Chemistry and Physics* 17, no. 19 (2017): 11849–11859, https://doi.org/10.5194/acp-17-11849-2017.

41. E. Herndon, A. AlBashaireh, D. Singer, T. Roy Chowdhury, B. Gu, and D. Graham, "Influence of Iron Redox Cycling on Organo-Mineral Associations in Arctic Tundra Soil," *Geochimica et Cosmochimica Acta* 207 (2017): 210–231, https://doi.org/10.1016/j.gca.2017.02.034.

42. A. Monhonval, J. Strauss, M. Thomas, et al., "Thermokarst Processes Increase the Supply of Stabilizing Surfaces and Elements (Fe, Mn, Al, and Ca) for Mineral–Organic Carbon Interactions," *Permafrost and Periglacial Processes* 33 (2022): 452–469, https://doi.org/10.1002/ppp.2162.

43. C. W. Mueller, C. Hoeschen, M. Steffens, et al., "Microscale Soil Structures Foster Organic Matter Stabilization in Permafrost Soils," *Geoderma* 293 (2017): 44–53, https://doi.org/10.1016/j.geoderma.2017.01.028.

44. K. Dutta, E. a. G. Schuur, J. C. Neff, and S. A. Zimov, "Potential Carbon Release From Permafrost Soils of Northeastern Siberia," *Global Change Biology* 12, no. 12 (2006): 2336–2351, https://doi.org/10.1111/j.1365-2486.2006.01259.x.

45. K. Kaiser and G. Guggenberger, "Mineral Surfaces and Soil Organic Matter," *European Journal of Soil Science* 54, no. 2 (2003): 219–236, https://doi.org/10.1046/j.1365-2389.2003.00544.x.

46. M. Kleber, K. Eusterhues, M. Keiluweit, C. Mikutta, R. Mikutta, and P. S. Nico, "Mineral–Organic Associations: Formation, Properties, and Relevance in Soil Environments," in *Advances in Agronomy*, vol. 130 (Elsevier, 2015), 1–140, https://doi.org/10.1016/bs.agron.2014.10.005.

47. K. Lalonde, A. Mucci, A. Ouellet, and Y. Gélinas, "Preservation of Organic Matter in Sediments Promoted by Iron," *Nature* 483, no. 7388 (2012): 198–200, https://doi.org/10.1038/nature10855.

48. C. C. Mu, T. J. Zhang, Q. Zhao, et al., "Soil Organic Carbon Stabilization by Iron in Permafrost Regions of the Qinghai-Tibet Plateau," *Geophysical Research Letters* 43, no. 19 (2016): 10,286–10,294, https://doi.org/10.1002/2016GL070071.

10991530, 0, Downloaded from https://onlinelibrary.wiley.com/doi/10.1002/ppp.70018 by Université De Liège, Wiley Online Library on [27/11/2025]. See the Terms and Conditions (https://onlinelibrary.wiley.com/terms-and-conditions) on Wiley Online Library for rules of use; OA articles are governed by the applicable Creative Commons License

49. C. Rumpel and I. Kögel-Knabner, "Deep Soil Organic Matter—A Key but Poorly Understood Component of Terrestrial C Cycle," *Plant and Soil* 338, no. 1 (2011): 143–158, https://doi.org/10.1007/s11104-010-0391-5.

50. Q. Li, W. Hu, L. Li, and Y. Li, "Interactions Between Organic Matter and Fe Oxides at Soil Micro-Interfaces: Quantification, Associations, and Influencing Factors," *Science of the Total Environment* 855 (2023): 158710, https://doi.org/10.1016/j.scitotenv.2022.158710.

51. O. Pokrovsky, J. Karlsson, and R. Giesler, "Freeze-Thaw Cycles of Arctic Thaw Ponds Remove Colloidal Metals and Generate Low-Molecular-Weight Organic Matter," *Biogeochemistry* 137, no. 3 (2018): 321–336, https://doi.org/10.1007/s10533-018-0421-6.

52. D. Adhikari and Y. Yang, "Selective Stabilization of Aliphatic Organic Carbon by Iron Oxide," *Scientific Reports* 5, no. 1 (2015): 11214, https://doi.org/10.1038/srep11214.

53. B. Ni, X. Yu, X. Duan, and Y. Zou, "Wetland Soil Organic Carbon Balance Is Reversed by Old Carbon and Iron Oxide Additions," *Frontiers in Microbiology* 14 (2024): 1327265, https://doi.org/10.3389/fmicb.2023.1327265.

54. X. Song, P. Wang, L. Van Zwieten, et al., "Towards a Better Understanding of the Role of Fe Cycling in Soil for Carbon Stabilization and Degradation," *Carbon Research* 1, no. 1 (2022): 5, https://doi.org/10.1007/s44246-022-00008-2.

55. A. C. Cismasu, K. H. Williams, and P. S. Nico, "Iron and Carbon Dynamics During Aging and Reductive Transformation of Biogenic Ferrihydrite," *Environmental Science & Technology* 50, no. 1 (2016): 25–35, https://doi.org/10.1021/acs.est.5b03021.

56. X. Huang, X. Liu, J. Liu, and H. Chen, "Iron-Bound Organic Carbon and Their Determinants in Peatlands of China," *Geoderma* 391 (2021): 114974, https://doi.org/10.1016/j.geoderma.2021.114974.

57. K. Kaiser, R. Mikutta, and G. Guggenberger, "Increased Stability of Organic Matter Sorbed to Ferrihydrite and Goethite on Aging," *Soil Science Society of America Journal* 71, no. 3 (2007): 711–719, https://doi.org/10.2136/sssaj2006.0189.

58. I. Slimani, X. Zhu-Barker, P. Lazicki, and W. Horwath, "Reviews and Syntheses: Iron—A Driver of Nitrogen Bioavailability in Soils?," *Biogeosciences* 20, no. 18 (2023): 3873–3894, https://doi.org/10.5194/bg-20-3873-2023.

59. S. M. Ilina, F. Poitrasson, S. A. Lapitskiy, Y. V. Alekhin, J. Viers, and O. S. Pokrovsky, "Extreme Iron Isotope Fractionation Between Colloids and Particles of Boreal and Temperate Organic-Rich Waters," *Geochimica et Cosmochimica Acta* 101 (2013): 96–111, https://doi.org/10.1016/j.gca.2012.10.023.

60. O. Pokrovsky and J. Schott, "Iron Colloids/Organic Matter Associated Transport of Major and Trace Elements in Small Boreal Rivers and Their Estuaries (NW Russia)," *Chemical Geology* 190, no. 1 (2002): 141–179, https://doi.org/10.1016/S0009-2541(02)00115-8.

61. O. Pokrovsky, J. Schott, and B. Dupré, "Trace Element Fractionation and Transport in Boreal Rivers and Soil Porewaters of Permafrost-Dominated Basaltic Terrain in Central Siberia," *Geochimica et Cosmochimica Acta* 70, no. 13 (2006): 3239–3260, https://doi.org/10.1016/j.gca.2006.04.008.

62. A. Chauhan, M. S. Patzner, A. Bhattacharyya, et al., "Interactions Between Iron and Carbon in Permafrost Thaw Ponds," *Science of the Total Environment* 946 (2024): 174321, https://doi.org/10.1016/j.scitotenv.2024.174321.

63. E. C. Rieb, C. A. Polik, G. W. Kling, and R. M. Cory, "Controls on the Apparent Quantum Yield for Photomineralization of Dissolved Organic Matter in Arctic Freshwaters," *Environmental Science: Processes & Impacts* 27 (2025): 2755–2769, https://doi.org/10.1039/D5EM00293A.

64. T. Rosswall, J. G. K. Flower-Ellis, L. G. Johansson, S. Jonsson, B. E. Ryden, and M. Sonesson, "Stordalen (Abisko), SWEDEN," *Ecological Bulletins* 20 (1975): 265–294.

65. J. Klaminder, K. Yoo, and R. Giesler, "Soil Carbon Accumulation in the Dry Tundra: Important Role Played by Precipitation," *Journal of Geophysical Research: Biogeosciences* 114, no. G4 (2009): 2009JG000947, https://doi.org/10.1029/2009JG000947.

66. M. Sonesson and E. Kvillner, "Plant Communities of the Stordalen Mire: A Comparison Between Numerical and Non-Numerical Classification Methods," *Ecological Bulletins* 30 (1980): 113–125.

67. T. V. Callaghan, F. Bergholm, T. R. Christensen, C. Jonasson, U. Kokfelt, and M. Johansson, "A New Climate Era in the Sub-Arctic: Accelerating Climate Changes and Multiple Impacts," *Geophysical Research Letters* 37, no. 14 (2010): 2009GL042064, https://doi.org/10.1029/2009GL042064.

68. H. J. Åkerman and M. Johansson, "Thawing Permafrost and Thicker Active Layers in Sub-Arctic Sweden," *Permafrost and Periglacial Processes* 19, no. 3 (2008): 279–292, https://doi.org/10.1002/ppp.626.

69. M. Palace, C. Herrick, J. DelGreco, R. Varner, D. Finnell, and A. J. Garnello, *Unmanned Aerial Imagery Over Stordalen Mire, Northern Sweden, 2014 (Version 1.0, p. 503328328) [Image/tiff]* (Harvard Dataverse, 2019), https://doi.org/10.7910/DVN/SJKV4T.

70. M. Palace, C. Herrick, F. Sullivan, and R. Varner, *Unmanned Aerial Imagery Over Stordalen Mire, Northern Sweden, 2022* (National Science Foundation, Trad.; V1 éd) (Harvard Dataverse, 2022), https://doi.org/10.7910/DVN/G9Y8WC.

71. J. P. Wilson and J. C. Gallant, eds., *Terrain Analysis: Principles and Applications* (Wiley, 2000).

72. N. Al-Sababhah, "Topographic Position Index to Landform Classification and Spatial Planning, Using GIS, for Wadi Araba, South West Jordan," *Environment and Ecology Research* 11, no. 1 (2023): 79–101, https://doi.org/10.13189/eer.2023.110106.

73. X. Zhou, L. Mou, T. Ao, X. Huang, and H. Yang, "Effect of the Spatial Resolution of Digital Terrain Data Obtained by Drone on Urban Fluvial Flood Modeling of Mountainous Regions," *Hydrology and Earth System Sciences* 29, no. 7 (2025): 1963–1980, https://doi.org/10.5194/hess-29-1963-2025.

74. D. Yeghicheyan, J. Carignan, M. Valladon, et al., "A Compilation of Silicon and Thirty One Trace Elements Measured in the Natural River Water Reference Material SLRS-4 (NRC-CNRC)," *Geostandards Newsletter* 25, no. 2–3 (2001): 465–474, https://doi.org/10.1111/j.1751-908X.2001.tb00617.x.

75. D. L. Parkhurst and C. A. J. Appelo, "PHREEQC (Version 3)," (2013).

76. C. R. Perryman, C. K. McCalley, A. Malhotra, et al., "Thaw Transitions and Redox Conditions Drive Methane Oxidation in a Permafrost Peatland," *Journal of Geophysical Research: Biogeosciences* 125, no. 3 (2020): e2019JG005526, https://doi.org/10.1029/2019JG005526.

77. D. Della Lunga, K. R. Brye, J. M. Slayden, C. G. Henry, and L. S. Wood, "Soil Moisture, Temperature, and Oxidation-Reduction Potential Fluctuations Across a Furrow-Irrigated Rice Field on a Silt-Loam Soil," *Journal of Rice Research and Developments* 3, no. 1 (2020): 103, https://scholars.direct/Articles/rice-research/jrrd-3-014.php?jid=rice-research.

78. E. Enanga, I. Creed, N. Casson, and F. Beall, "Summer Storms Trigger Soil N 2 O Efflux Episodes in Forested Catchments," *Journal of Geophysical Research: Biogeosciences* 121 (2016): 95–108, https://doi.org/10.1002/2015JG003027.

79. G. Neumann and V. Römheld, "Chapter 14—Rhizosphere Chemistry in Relation to Plant Nutrition," in *Marschner's Mineral Nutrition of Higher Plants*, Third ed., ed. P. Marschner (Academic Press, 2012), 347–368, https://doi.org/10.1016/B978-0-12-384905-2.00014-5.

80. J. P. Gustafsson, "Visual MINTEQ (Version 3.1: A Windows Version of MINTEQA2)" (2011).

10991530, 0, Downloaded from https://onlinelibrary.wiley.com/doi/10.1002/ppp.70018 by Université De Liège, Wiley Online Library on [27/11/2025]. See the Terms and Conditions (https://onlinelibrary.wiley.com/terms-and-conditions) on Wiley Online Library for rules of use; OA articles are governed by the applicable Creative Commons License

81. R. Marsac, C. Catrouillet, M. Pédrot, et al., "Equilibrium Surface Complexation Modeling With Metastable Natural Colloids: The Key to Predict the Oxidation State Distribution of Trace Elements?," *Current Opinion in Colloid & Interface Science* 72 (2024): 101820, https://doi.org/10.1016/j.cocis.2024.101820.

82. C. S. Sjöstedt, J. P. Gustafsson, and S. J. Köhler, "Chemical Equilibrium Modeling of Organic Acids, pH, Aluminum, and Iron in Swedish Surface Waters," *Environmental Science & Technology* 44, no. 22 (2010): 8587–8593, https://doi.org/10.1021/es102415r.

83. H. Rodenhizer, J. Ledman, M. Mauritz, et al., "Carbon Thaw Rate Doubles When Accounting for Subsidence in a Permafrost Warming Experiment," *Journal of Geophysical Research: Biogeosciences* 125, no. 6 (2020): e2019JG005528, https://doi.org/10.1029/2019JG005528.

84. R. Lindsay, "Peatland (Mire Types): Based on Origin and Behavior of Water, Peat Genesis, Landscape Position, and Climate," in *The Wetland Book*, eds. C. M. Finlayson, G. R. Milton, R. C. Prentice, and N. C. Davidson (Springer Netherlands, 2018b), 251–273, https://doi.org/10.1007/978-94-007-4001-3_279.

85. J. Holden, "Peatland Hydrology and Carbon Release: Why Small-Scale Process Matters," *Philosophical Transactions of the Royal Society A: Mathematical, Physical and Engineering Sciences* 363, no. 1837 (2005): 2891–2913.

86. H. Liu and B. Lennartz, "Hydraulic Properties of Peat Soils Along a Bulk Density Gradient—A Meta Study," *Hydrological Processes* 33 (2019): 101–114, https://doi.org/10.1002/hyp.13314.

87. M. W. Menberu, H. Marttila, A.-K. Ronkanen, A. T. Haghighi, and B. Kløve, "Hydraulic and Physical Properties of Managed and Intact Peatlands: Application of the van Genuchten-Mualem Models to Peat Soils," *Water Resources Research* 57, no. 7 (2021): e2020WR028624, https://doi.org/10.1029/2020WR028624.

88. W. L. Quinton, M. Hayashi, and L. E. Chasmer, "Peatland Hydrology of Discontinuous Permafrost in the Northwest Territories: Overview and Synthesis," *Canadian Water Resources Journal = Revue Canadienne Des Ressources Hydriques* 34, no. 4 (2009): 311–328, https://doi.org/10.4296/cwrj3404311.

89. M. Barczok, C. Smith, L. Kinsman-Costello, et al., "Iron Transformation Mediates Phosphate Retention Across a Permafrost Thaw Gradient," *Communications Earth & Environment* 5, no. 1 (2024): 1–11, https://doi.org/10.1038/s43247-024-01810-z.

90. E. C. Rooney, E. VanderJeugdt, S. Avasarala, et al., "Decoupling of Redox Processes From Soil Saturation in Arctic Tundra," *Communications Earth & Environment* 5, no. 1 (2024): 1–9, https://doi.org/10.1038/s43247-024-01927-1.

91. X. Huang, X. Liu, L. Chen, Y. Wang, and H. Chen, "Iron-Bound Organic Carbon Dynamics in Peatland Profiles: The Preservation Equivalence of Deep and Surface Soil," *Fundamental Research* 3, no. 6 (2023): 852–860, https://doi.org/10.1016/j.fmre.2022.09.026.

92. S. Li, S. Chen, M. Wang, et al., "Redistribution of Iron Oxides in Aggregates Induced by pe + pH Variation Alters Cd Availability in Paddy Soils," *Science of the Total Environment* 752 (2021): 142164, https://doi.org/10.1016/j.scitotenv.2020.142164.

93. C. Hirst, E. Mauclet, A. Monhonval, et al., "Seasonal Changes in Hydrology and Permafrost Degradation Control Mineral Element-Bound DOC Transport From Permafrost Soils to Streams," *Global Biogeochemical Cycles* 36, no. 2 (2022): e2021GB007105, https://doi.org/10.1029/2021GB007105.

94. T. V. Raudina, S. V. Loiko, A. G. Lim, et al., "Dissolved Organic Carbon and Major and Trace Elements in Peat Porewater of Sporadic, Discontinuous, and Continuous Permafrost Zones of Western Siberia," *Biogeosciences* 14, no. 14 (2017): 3561–3584, https://doi.org/10.5194/bg-14-3561-2017.

95. I. Fedorova, A. Chetverova, D. Bolshiyanov, et al., "Lena Delta Hydrology and Geochemistry: Long-Term Hydrological Data and Recent Field Observations," *Biogeosciences* 12, no. 2 (2015): 345–363, https://doi.org/10.5194/bg-12-345-2015.

96. S. W. Reeder, B. Hitchon, and A. A. Levinson, "Hydrogeochemistry of the Surface Waters of the Mackenzie River Drainage Basin, Canada—I. Factors Controlling Inorganic Composition," *Geochimica et Cosmochimica Acta* 36, no. 8 (1972): 825–865, https://doi.org/10.1016/0016-7037(72)90053-1.

97. D. M. Rosenberg, D. R. Barton, G. J. Brunskill, and P. J. McCart, "The Mackenzie River System," in *The Ecology of River Systems*, vol. 60, ed. B. R. Davies and K. F. Walker (Springer Netherlands, 1986), 425–540, https://doi.org/10.1007/978-94-017-3290-1_10.

98. S. N. Vorobyev, J. Karlsson, Y. Y. Kolesnichenko, M. A. Korets, and O. S. Pokrovsky, "Fluvial Carbon Dioxide Emission From the Lena River Basin During the Spring Flood," *Biogeosciences* 18, no. 17 (2021): 4919–4936, https://doi.org/10.5194/bg-18-4919-2021.

99. P. J. Blaen, A. M. Milner, D. M. Hannah, J. E. Brittain, and L. E. Brown, "Impact of Changing Hydrology on Nutrient Uptake in High Arctic Rivers," *River Research and Applications* 30, no. 9 (2014): 1073–1083, https://doi.org/10.1002/rra.2706.

100. M. Diak, M. E. Böttcher, C. M. Ehlert von Ahn, et al., "Permafrost and Groundwater Interaction: Current State and Future Perspective," *Frontiers in Earth Science* 11 (2023): 1254309, https://doi.org/10.3389/feart.2023.1254309.

101. W. Stumm and J. J. Morgan, *Aquatic Chemistry: Chemical Equilibria and Rates in Natural Waters* (John Wiley & Sons, 1996).

102. L. E. Street, J. F. Dean, M. F. Billett, et al., "Redox Dynamics in the Active Layer of an Arctic Headwater Catchment; Examining the Potential for Transfer of Dissolved Methane From Soils to Stream Water," *Journal of Geophysical Research: Biogeosciences* 121, no. 11 (2016): 2776–2792, https://doi.org/10.1002/2016JG003387.

103. E. Neubauer, W. D. C. Schenkeveld, K. L. Plathe, et al., "The Influence of pH on Iron Speciation in Podzol Extracts: Iron Complexes With Natural Organic Matter, and Iron Mineral Nanoparticles," *Science of the Total Environment* 461-462 (2013): 108–116, https://doi.org/10.1016/j.scitotenv.2013.04.076.

104. R. M. Cory, C. P. Ward, B. C. Crump, and G. W. Kling, "Sunlight Controls Water Column Processing of Carbon in Arctic Fresh Waters," *Science* 345, no. 6199 (2014): 925–928, https://doi.org/10.1126/science.1253119.

105. G. Rocher-Ros, T. K. Harms, R. A. Sponseller, M. Väisänen, C.-M. Mörth, and R. Giesler, "Metabolism Overrides Photo-Oxidation in CO_2 Dynamics of Arctic Permafrost Streams," *Limnology and Oceanography* 66, no. S1 (2021): S169–S181, https://doi.org/10.1002/lno.11564.

106. P. J. Mann, T. I. Eglinton, C. P. McIntyre, et al., "Utilization of Ancient Permafrost Carbon in Headwaters of Arctic Fluvial Networks," *Nature Communications* 6 (2015): 7856, https://doi.org/10.1038/ncomms8856.

107. H. Xie, O. C. Zafiriou, W.-J. Cai, R. G. Zepp, and Y. Wang, "Photooxidation and Its Effects on the Carboxyl Content of Dissolved Organic Matter in Two Coastal Rivers in the Southeastern United States," *Environmental Science & Technology* 38, no. 15 (2004): 4113–4119, https://doi.org/10.1021/es035407t.

108. O. V. Oleinikova, L. S. Shirokova, E. Gérard, et al., "Transformation of Organo-Ferric Peat Colloids by a Heterotrophic Bacterium," *Geochimica et Cosmochimica Acta* 205 (2017): 313–330, https://doi.org/10.1016/j.gca.2017.02.029.

Supporting Information

Additional supporting information can be found online in the Supporting Information section. **Figure S1:** Orthomosaic clips of the palsa (a) and degraded palsa (b) sites at Stordalen mire from July 2016 and July 2022 (Palace et al. 2019, 2022). Red circles indicate the exact location of the

10991530, 0, Downloaded from https://onlinelibrary.wiley.com/doi/10.1002/ppp.70018 by Université De Liège, Wiley Online Library on [27/11/2025]. See the Terms and Conditions (https://onlinelibrary.wiley.com/terms-and-conditions) on Wiley Online Library for rules of use; OA articles are governed by the applicable Creative Commons License

sampling locations A, B, and C within each picture. **Figure S2:** (a) Soil temperature (°C) and (b) Soil water content (m^3/m^3) at 10 cm (gray) and 30 cm (black) in function of time measured every 10 min at the palsa and the intermediate sites between September 20 and October 7, 2021. The same measurements were made at the degraded palsa site at 10 cm on four occasions (27–09-21, 30–09-21, 04–10-21, and 07–10-21) during the sampling campaign. **Figure S3:** Soil redox potential (mV) measured at 12.5 and 30 cm depth at the intermediate site between September 20 and October 7, 2021. **Table S1:** Input (pH, redox (mV), and concentration in Fe (μg/L)) and output (concentrations in Fe^{2+} and Fe^{3+}) of the geochemical modeling (PHREEQC) made on soil pore waters collected at the palsa, the intermediate (location A, B, and C), and the degraded palsa sites at 10 and 30 cm depth.

10991530, 0, Downloaded from https://onlinelibrary.wiley.com/doi/10.1002/ppp.70018 by Université De Liège, Wiley Online Library on [27/11/2025]. See the Terms and Conditions (https://onlinelibrary.wiley.com/terms-and-conditions) on Wiley Online Library for rules of use; OA articles are governed by the applicable Creative Commons License